國立交通大學

光電工程研究所

碩士論文

氮化鎵面射型雷射與極激子在多模氮化鎵微共振腔內色散的光學特性研究

Optical Characteristics of GaN-based Vertical Cavity Surface Emitting Lasers and Cavity Polariton Dispersion in Multimode GaN Microcavity

研究生：劉玫君

指導教授：郭浩中 教授

盧廷昌 教授

中華民國九十八年七月

氮化鎵面射型雷射與極激子在多模氮化鎵微共振腔內色散的光學特性研究

Optical Characteristics of GaN-based Vertical Cavity Surface Emitting Lasers and Cavity Polariton Dispersion in Multimode GaN Microcavity

研究生：劉玫君	Student：Mei-Chun Liu
指導教授：郭浩中 教授	Advisor：Prof. Hao-Chung Kuo
盧廷昌 教授	Prof. Tien-Chang Lu

國立交通大學 電機資訊學院

光電工程研究所

碩士論文

A Thesis

Submitted to Institute of Electro-Optical Engineering

College of Electrical Engineering and Computer Science

National Chiao Tung University

in Partial Fulfillment of the Requirements

for the Degree of

Master

In

Electro-Optical Engineering

July 2009

Hsinchu, Taiwan, Republic of China

中華民國 九十八 年 七 月

氮化鎵面射型雷射與極激子在多模氮化鎵微共振腔內色散的光學特性研究

研究生: 劉玫君　　　　　　　　　指導教授: 郭浩中 教授

盧廷昌 教授

國立交通大學光電工程研究所

摘要

由於, 以氮化鎵所混合而成的半導體基材具有從0.7到6.2電子伏特的寬廣能隙和其直接能隙的特性，使其發光波長範圍能從紅外光到紫外光並且發光效率也比較高。因其以上特性，使得氮化鎵基材發光元件可廣泛應用，故其成為世界上各研發團體的重要研究課題之一。在此研究論文中，我們製作氮化鎵面射型雷射（VCSEL），並研究分析其主要的特性。

於此，我們提出含有上下兩高反射鏡介電質之氮化鎵面射型雷射結構。並利用雷射剝離技術並沉積成長介電質反射鏡，製作出一含有氮化鎵與氮化銦鎵（GaN/InGaN）多量子井(MQW)的面射型結構。在室溫下以一雷射(波長為355 nm)為激發光源，在光激發操作下，研究其發光特性。此氮化鎵面射型雷射的Q係數(quality factor)為1000，雷射波長為 412 nm，雷射頻譜之半高寬為 0.26 nm。從實驗中，我們可以得到雷射頻譜之極化率為 79.4 %和其發散角為5度。此氮化鎵面射型雷射於室溫下之臨界條件為 784 nJ且其特徵溫度為 130 K。

我們利用 Hakki-Paoli 方法和量測不同溫度下的頻譜，並計算求得此面射型雷射的增益特性。在 80 K臨界條件時，光增益為 2.2×10^{3} cm^{-1}。在不同操作溫度下，我

們發現溫度越低，光增益隨著注入的載子數目增加而變大的速率越快。線寬增加係數（linewidth enhancement factor）在室溫下為 4.3，其值隨著操作溫度下降而降低，直至溫度為 80 K時，其也降至0.6了。利用微螢光激發 (micro-PL)方式量測發現在雷射發光孔徑中有螢光強度不均勻的現象，並對其發光強度不同的位置各自量測並計算其增益的特性。發現，螢光強度較強的位置得到的增益值比在較弱位置的大，並由其增益的頻譜圖觀察到，波長從 400 nm到 420 nm的增益斜率比較大，而波長從 420 nm到 445 nm的增益斜率趨於平緩。

另外，在實驗過程中觀察到一個特別的現象，從波長 470 nm到 370 nm的範圍中，發現其模態間距（mode spacing）有漸漸變小的趨勢。故我們利用材料本身的折射率色散和極激子（polariton）的色散去對其共振模態作曲線的吻合程度,發現極激子的色散曲線比較吻合。

Optical Characteristics of GaN-based Vertical Cavity Surface Emitting Lasers and Cavity Polariton Dispersion in Multimode GaN Microcavity

Student: Mei-Chun Liu **Advisor: Prof. Hao-Chung Kuo**

Prof. Tien-Chang Lu

Institute of Electro-Optical Engineering, National Chiao Tung University

Abstract

Due to the inherent advantages of GaN-based compound materials, such as wide band gap varying from 0.7 to 6.2eV、direct band gap characteristics…, etc. Which all make them possible to emit emission wavelength ranging from red to ultra-violet with higher illumination. Therefore, GaN-based semiconductors have recently attracted much interest owing to their applications in optoelectronics devices. In this study, the fabrication of GaN-based vertical cavity surface emitting lasers (VCSELs) is analyzed and characterized.

We proposed a GaN-based VCSEL structure which consists of InGaN/GaN MQWs and two dielectric DBRs with high reflectivity. We investigated the laser emission characteristics of the GaN-based VCSEL under optically pumping operation at room temperature. The quality factor of VCSEL is 1000, indicating a good interfacial layer quality of the structure. The laser emits emission wavelength at 412 nm with a linewidth of 0.26 nm. The measurement results reveal the linewidth reduction, degree of polarization of 79.4%, and the divergent angle of 5°. The laser has a threshold pumping energy of 784 nJ at room temperature and the characteristic temperature is 130K.

Meanwhile, we used Hakki-Paoli method and the measured photoluminescence spectrum to estimate the temperature dependent optical gain and linewidth enhancement factor of the VCSELs. At 80 K, the optical gain of 2.2×10^{3} cm^{-1} was estimated at the threshold condition with a carrier density of 6.8×10^{19} cm^{-3} by pulse laser. We found that the gain increases more rapidly as a function of the injected carrier density at lower temperature by two difference pumping sources. The α-factor at 300 K was estimated to be 4.3 and decreased to as low as 0.6 at 80 K. Micro-PL intensity mapping indicated that there exists nonuniform PL emission intensity over the VCSEL aperture. The gain values of the highest PL intensity are larger than the ones of lower PL intensity. We obtained the sharp slope of gain spectrum from 400 nm to 420 nm, while the slope of the gain spectrum ranging from 420 nm to 445 nm is smooth.

The frequency spacing between adjacent PL peaks decreases by almost a factor of five from 470 nm to 370 nm. We use the intrinsic material index dispersion and polariton dispersion to fit the experimental data, it shows that the latter fitting curve is much better than the former one.

Acknowledgement

時光飛逝，在碩士班的兩年內，不管是在學業、研究和生活方面，都得到許多人的指導與協助。首要感謝實驗室的老師們—王老師、郭老師、盧老師，王老師爽朗的笑聲總是充斥著整個實驗室，替我們帶來很多歡樂與鼓勵；郭老師平時總是和我們聊天，並適時給予鼓勵和要求，期達到學術研究的完整性；盧老師對實驗進度的要求並教導我如何運用物理機制去分析數據以達到合理的解釋，讓我學習到很多知識。並且要感謝中研院的程老師，從我碩一開始，就慢慢灌輸我很多學識並教導我應用到研究上，還和我一起做實驗到很晚，一直到我畢業還是不停的在教導我更多知識。

還要感謝當初在我剛進實驗室，就開始帶領我學習儀器和有關研究方面的基本觀念的小朱學長，雖然我升碩二時，學長就畢業了，但其還會時常關心我的進度，甚至有問題時，學長還會說明給我聽；也要感謝明華學長帶領我架設量測系統並教導我如何從零到完整的系統出來，一個多月以來，每天架到凌晨三點的辛勞，令人難以忘懷；還有俊榮學長在我研究上的幫助，學長時常幫助我分析數據、檢查每次咪聽要報告的資料，還有一起架設影像系統，令人萬般感激；還有啄木在課業研究和心靈上，給予我很多的幫助；加上柏孝、世杰和輝閔學長，還有小馬、政暐、小柯、睿中、阿綱、智凱、勁生、尚樺、永吉、詳祺、重卿、伊嚀、惟雯，很開心能和你們在實驗室相遇，一起度過很多歡笑和淚水的日子，期待往後大家都能更順心。

最後，還要感謝我的父母、親人和朋友，在我不順利的時候，一直給予我前進的力量。感謝大家的幫忙，讓我能完成我的碩士學業。

Contents

Abstract (in Chinese)…………….…………………..………......I

Abstract (in English)……………………….………………III

Acknowledgement……………………………...……………....V

Contents…………………………………...………….........VI

List of Figures..IX

Chapter 1 Introduction and Motivation……………………………1

1.1 GaN-based materials and motivation………………………………1

1.2 GaN-based laser diodes…………..3

1.3 GaN-based laser microcavities……………………………………..5

1.4 An overview of the thesis…………………………………...…...6

Reference……………………………………………………………9

Chapter 2 Fundamental of GaN-based vertical cavity surface emitting lasers and semiconductor microcavities……………………………15

2.1 Vertical cavity surface emitting lasers…………….........................15

2.1.1 Fundamental of VCSELs……………………………………...15

2.1.2 Distributed Bragg reflector…………………………………....17

2.2 Fundamental of semiconductor microcavities……………………..23

2.2.1 polariton dispersion curve in the strong coupling regime…....…23

2.2.2 Bose Einstein condensation…………………….........................28

Reference...34

Chapter 3 Characteristics of the two dielectric DBR GaN-VCSELs ……………………………………………………………………...37

3.1 Structure design……………………………………………………...37

3.1.1 GaN-based VCSELs with two mirrors…………………………..37

3.1.2 Laser lift-off technique……………………………………………38

3.1.3 Sample structure…………………………………………………39

3.2 Measurement setup………………………………………………..…40

3.3 Threshold condition and spectrum evolution……………………..…41

3.4 Temperature characteristic…………………………………………43

3.5 The gain characteristics for different temperature……………………44

3.5.1 Temperature dependent gain characteristics by a Nd: yttrium aluminum garent (YAG) laser……………………………………..……44

3.5.2 Temperature dependent gain characteristics by a CW laser…..…47

Reference………………………………………………………………64

Chapter 4 Characteristics of semiconductor microcavity…………….65

4.1 Sample structure and measurement setup………………………..…65

4.2 Strong cavity polariton dispersion in multimode GaN microcavity…..65

Reference…………………………………………………………………75

Chapter 5 Conclusions and Future Work………………………..…..76

5.1 Conclusion………………………………………………………..….76

5.1.1 Two dielectric DBRs VCSELs…………………………….…......76

5.1.2 Cavity polariton dispersion in multimode GaN microcavity…....77

5.2 Future works……………………………………………………....77

List of figures

Chapter 1

Figure 1.1 Lattice constant as s function of band gap energy of III-V nitride compounds………………………………………………………..8

Figure 1.2 (a) Schematic structure of EEL. (b) Schematic structure of VCSEL……………………………………………………………………...8

Chapter 2

Figure 2.1 Basic geometry of a vertical cavity surface emitting laser…30

Figure 2.2 A typical microcavity structure. The central cavity layer having a thickness equal to an integer number of half-wave-lengths of light at the exciton resonance frequency is sandwiched between two Bragg mirrors. A quantum well (several quantum wells) should be embedded in the antinodes of the cavity mode electric field in order to provide the strongest coupling to light………………………………......................................30

Figure 2.3 Schematic draw of the light reflected from the top and bottom of the thin film…………………………………………………………..31

Figure 2.4 Schematic of distributed Bragg reflector incorporating m pairs of two mediums with indices n_1 and n_2……………………………………31

Figure 2.5 Reflectance of an $\lambda/2$ empty microcavity………………..32

Figure 2.6 Polaritons are produced by interaction between excitons and photons……………………………………………………………...…..32

Figure 2.7 When the exciton state is strongly coupled to the cavity-photon mode, quasi-particle called cavity polaritons are produced with an anti-crossing dispersion relation………………………………..…33

Figure 2.8 Polariton dispersion for different detuning between exciton and photon modes: (a) δ= positive, (b) δ= zero, (c) δ= negative. Dashed lines show the energies of uncoupled exciton and photon modes……………........33

Chapter 3

Figure 3.1 The simulated standing wave patterns inside the cavity for the dielectric DBRs VCSEL structure………………………………………………49

Figure 3.2 Measure spectral reflectivity of 6 pairs of SiO_2/TiO_2 DBR and 8 pairs of SiO_2/Ta_2O_5 DBR. The PL spectrum of the as grown cavity consists of 10 pairs of 5 nm GaN barriers and 3 nm $In_{0.1}Ga_{0.9}N$ wells…………..…49

Figure 3.3 The layer structure used for calculation of standing wave patterns. The structure was constructed according to the fabricated dielectric DBRs VCSELs………………………………………………………………50

Figure 3.4 Fabrication of the GaN-based dielectric DBRs VCSEL…..51

Figure 3.5 (a) The left picture is the microscopic image of a fabricated 2x2 VCSEL array. The circular areas are the locations of VCSELs with DBRs, also serving the emission apertures. (b)、(c) A photograph of the fabricated VCSEL on a silica host substrate and a Si substrate, respectively……………………………………………………………...52

Figure 3.6 Schematic disgram of measurement setup for the characteristics of the GaN-based two dielectric DBRs VCSEL…………..…..53

Figure 3.7 Spontaneous emission spectrum below threshold condition shows multiple cavity modes……………………………………………...53

Figure 3.8 Spectral evolution of the VCSEL emission different pumping levels………………………………………………………………………54

Figure 3.9 Laser emission intensity obtained from the emission spectra as a function of pumping energy at room temperature. The inset represents one of the lasing conditions, whose pumping power is 0.89mW.…………54

Figure 3.10 Far field pattern of the VCSEL………………………...…55

Figure 3.11 The angle dependent laser intensity………………………55

Figure 3.12 Temperature dependence of the lasing threshold of the VCSEL…………………………………………………………………..…56

Figure 3.13 Photoluminescence spectra of the GaN-based VCSEL under different pumping power levels at 80 K……………………...…………57

Figure 3.14 Gain spectra of the VCSEL under different pumping power levels at 80 K…………………………………………………………..…57

Figure 3.15 Pumping carrier density dependence of the peak gain of the lasing mode for different temperature…………………………………..58

Figure 3.16 The α-factor value at different temperature temperature…58

Figure 3.17 (a) Micro-PL intensity mapping image of the VCSEL aperture. (b) Fine micro-PL scan inside the square area in (a)……………59

Figure 3.18 PL spectra of highest PL intensity point (A) and the lower PL intensity point (B)……………………………………………………..…60

Figure 3.19 Photoluminescence spectra of the GaN-based VCSEL under different pumping power levels at 80k (a) the bright areas (A), (b) the dark areas (B)……………………………………………………………..……61

Figure 3.20 Gain spectra of the VCSEL under different pumping power levels at 80k.(a) the bright areas (A), (b) the dark areas (B)……..………62

Figure 3.21 Pumping carrier density dependence of the peak gain of the lasing mode for different temperature (a) the bright areas (A), (b) the dark areas (B)……………………………………………………………..…63

Chapter 4

Figure 4.1 Schematic diagram of measurement setup……..………69

Figure 4.2 The PL spectra of optically pumped GaN/InGaN surface emitting microcavity (a) PL spectra at various pump power levels. The GaN and InGaN/GaN QW transitions are both excited. The resonant spacing decreases by almost a factor of five from 470 nm to 370 nm. (b) A zoom in spectrum around GaN transition wavelength region. (c) (d) Typical multiple

Lorentzian profile fitting along with the sums of the fitted profiles superimposed on PL spectra……………………………………………70

Figure 4.3 Phase shift and reflectance of DBR……………….………72

Figure 4.4 The index of refraction measured by ellipsometer (blue curve) is fitted by a theoretical index dispersion equation (red curve)……………72

Figure 4.5 The effective index from PL resonant peaks (blue square legend) are fitted by a theoretical index dispersion equation (red curve)…73

Figure 4.6 The red square legends are the observed multimode energy positions plotted versus equally spaced wave numbers. The blue line is the fitted curve based on cavity polariton dispersion equation. The two straight lines are the exciton and photon energies obtained from fitting parameters. The black triangle legends are the corresponding cavity photon modes….74

Chapter 1

Introduction and Motivation

1.1 GaN-based materials and motivation

Group III-nitride wide-band-gap semiconductors have recently attracted considerable interest owing to their applications in optoelectronics devices, such as blue-light-emitting diodes (LEDs) and laser diodes (LDs). GaN based-compound in optical devices that are active in the blue/green and ultraviolet (UV) wavelength regions make it a compelling material system for electronic devices capable of operating at high temperature, high power levels, and in harsh environments. In 1993, the first prototype high brightness GaN-based blue LEDs were developed by Nakamura's group, also they developed the first GaN-based violet LD with an emission wavelength of around 400nm in 1996. From that time, research groups in the laboratories and companies have spent more time on the development of GaN-based devices and many commercial products with various applications were produced. Today, bright blue LEDs based on III-nitrides paved the way for full-color display as well as for the mixing of the three primary colors to obtain white light for illumination by semiconductor LEDs. Short-wavelength LDs based on III-nitrides are essential for high-density optical storage applications because the diffraction-limited optical storage density increases quadratically as the probe laser wavelength is reduced. GaN-based shot-wavelength devices, such as blue LEDs and LDs, are required for a number of applications including solid-state lighting, full-color electroluminescent displays, laser printers, read-write laser sources for high-density information storage on magnetic and optical media, and sources for short-distance optical communications. The solid-state lighting is the most high-profile and desired application of the GaN-based materials due to the high luminescence efficiency, reliability and durability of the semiconductor light-emitting devices.

As demonstrated by III-nitride bright blue LEDs and LDs, all III-nitride-based devices must take advantage of heterojunctions and QWs. InGaN and AlGaN are direct band gap semiconductor alloys with energy band gap varying from 0.7 to 3.4 eV (InGaN) and 3.4 to 6.2 eV (AlGaN), with a predominant wurtzite structure for both alloys at all composition, as shown in Figure 1.1. Thus, red- to ultraviolet-emitting devices are possible to be fabricated by using AlGaInN. It is well known that localized exciton recombination is the dominant optical process in many semiconductor alloys at low temperature, including CdSSe, GaAsP, and CdMnTe alloys. The unique properties of III-nitrides make them have many particularly problems in growth, characterization, and device fabrications. Substrate is an important issue for III-V ntride material growth. Comparing to the GaAs material system, GaN-based substrate generally have a large lattice mismatch. Due to the lack of GaN substrates, III-nitride epilayers are most commonly grown on SiC or sapphire substrates, which contain a high dislocation density of the order of 10^8~10^{10}/cm^2. Nevertheless, SiC is more proper than sapphire for the substrate for GaN since it has small lattice mismatch. However, the cost of a SiC substrate is very expensive. Therefore, sapphire becomes a suitable and alternative substrate for GaN growth. The first progress used AlN [1.1, 1.2] or GaN [1.3, 1.4] nucleation layers to get high-quality GaN films including of high mobility and strong photoluminescence (PL) intensity. For the LEDs and LDs p/n layers are used to inject holes and electrons into the active layers, therefore, both p-type and n-type conductivity control are required to fabricate those devices. N-type GaN was easy to form but it was impossible to obtain p-type GaN films for a long period [1.5, 1.6]. Nevertheless, Amano et al [1.7] in 1989 and Nakamura et al [1.8, 1.9] in 1992 obtained the low-resistivity p-type GaN films. Optical properties of III-nitride quantum wells (QWs) are more complicated in comparison with other better understood III-V QWs due to the lack of GaN substrates and the large energy band gap offset and lattice mismatch between the well and the barrier materials. The main progress was the growth of InGaN film which is the most important compound semiconductor among III–V nitride compounds because InGaN active layers emit light by the recombination of the injected electrons and holes in the InGaN. An InGaN multiquantum-well (MQW) structure and confirmed an enhanced strong PL intensity from the quantized energy levels of the InGaN well layer with a thickness of 25 Å for the first time [1.10]. A small amount of indium added to the GaN could result a strong band-to-band emission from green to ultraviolet (UV) by changing the In content of InGaN. While the GaN without indium cannot emit a strong band-to-band emission at room-temperature. Therefore, indium content is very important which reason is considered to be related to deep localized energy states [1.11-1.15].

Many efforts were done on improving the internal quantum efficiency (IEQ) and light extraction efficiency (LEE) of GaN-based LEDs. Therefore, how to reduce the dislocation or defect and improve the light extraction efficiency is an important issue. For example, textured or roughtened surfaces [1.16], substrate shaping [1.17], thin-film LED [1.18], flip-chip LED [1.19] and photonic crystal on LED [1.20], ect.

1.2 GaN-based laser diodes

At present, the main focus of III-V nitride research is to develop a commercially viable current-injection laser diode which operates by continuous-wave (CW) at room temperature. Recent developments have yielded on optically pumped stimulated emission from GaN films [1.21, 1.22], InGaN films [1.23-1.26], AlGaN/InGaN double heterostructures [1.27] and GaN/AlGaN double heterostructures [1.28, 1.29]. The RT violet edge-emitting laser (EEL) with InGaN MQW GaN/AlGaN-based heterostructures under pulsed operation were achieved [1.30]. After that, many groups have reported pulsed operation of EELs [1.31-1.38] and high-power LDs fabricated using epitaxially laterally overgrown GaN (ELOG) [1.39] and GaN substrates [1.40]. Also, owing to ensuing continual advances in GaN technology, optically [1.23, 1.41-1.47] and electrically [1.48, 1.49] pumped GaN-based Vertical-cavity surface-emitting lasers (VCSELs) have been reported at low and room temperature.

VCSELs are different from EELs in device structure, it is another type of semiconductor lasers. The optical cavity length of VCSELs and EELs are of about 1 μm and 300 μm respectively. Therefore, VCSEL structures can emit a single longitudinal mode with a symmetrically circular beam due to a smaller optical mode volume compared to the EELs. Recently, the realization of GaN-based blue-violet-light VCSELs has attracted much attention because of their many advantages over EELs, including a circular beam, a small beam divergent angle, light emission in the vertical direction, and two-dimensional arrays at the wafer level, as shown in Figure 1.2. In particular, the use of two-dimensional arrays of the blue VCSEL could reduce the read-out time in high density optical storage and increase the scan speed in high-resolution laser printing technique. Several groups have reported optically pumped GaN-based VCSELs using different kinds of vertical resonant cavity structure [1.50-1.59]. VCSELs in many respects outperform EELs diodes. These devices have already become the dominating transmitter source for commercial high-speed optical interconnects operating in the 800 to 1000nm wavelength regime, and the emergence of 1.3 and 1.55 μm long-wavelength VCSELs on the market is eagerly awaited. Additionally, the strong field in the VCSEL microcavity can facilitate the investigation of the cavity quantum electrodynamics effect such as single photon and polariton emission, controlled spontaneous emission, and low threshold or thresholdless lasing [1.60-1.62].

1.3 GaN-based laser microcavities

A typical microcavity (MC) consists of a few half wavelength lengths cavity and a pair of high-reflectivity distributed Bragg mirrors (DBRs) are necessary for reducing lasing threshold. The planar semiconductor MCs in the strong coupling regime [1.63] have attracted a good deal of attention owing to their potential to enhance and control the interaction between photons and excitons, which leads to cavity polaritons. Beyond the standard VCSELs mentioned above, another type of laser, polariton laser is very attractive owing to its nearly thresholdless operation through Bose-Einstein condensation using cavity polaritons whose genesis lies in the interaction between photons and excitons. Polariton lasers have attracted much attention because of their many advantages over conventional lasers, including the reason that light is emitted by a macroscopic population of exciton-polaritons accumulated in the lowest energy state of their spectrum due to stimulated scattering. Note that no population inversion is needed in a polariton laser. Polariton lasers, MC structures, operative in the strong coupling regime can produce ultra-coherent light. Emission of photons by a polariton laser is a tunneling effect: light passes through a mirror from inside the cavity (where it is incorporated in an exciton-polariton condensate) to outside the cavity (where it becomes conventional light composed of free photons). Thus, polariton lasers have no threahold linked to the population inversion. Amplification of light in polariton lasers is governed by the ratio between the lifetime of exciton polaritons and their relaxation time towards the condensate. This relaxation has a stimulated character in polariton lasers, which is why it can be quite rapid.

Polariton lasing at high temperatures requires other material systems in which excitons actually survive at that temperature. The semiconductor-based MCs such as GaN came to attract increasing attention to room temperature polariton devices, such as polariton lasers, polariton LEDs, and polariton parametric amplifiers owing to the large exciton binding energies and oscillator strengths. Recently, room temperature polariton lasing has been observed in a bulk-GaN MC [1.64], and multi quantum well (MQW) MC [1.65]. Since the study of polariton induced nonlinear phenomena is in its early stage, electrically injected polariton lasers are awaiting further development. However, the optically pumped experiments, which have been successful, form the stepping stone for electrical injection.

1.4 An overview of the thesis

Chapter 2 outlines the GaN-based VCSEL. We fabricating a GaN-based VCSEL and overview the three main types of propertied GaN-based VCSELs. The reasons for using VCSEL structure with two dielectric mirrors in the thesis are presented. We presents the structure and designing issues of the GaN-based VCSELs with two dielectric mirrors. The spectral reflectivity of the SiO_2/TiO_2 and SiO_2/Ta_2O_5 DBRs are calculated by transfer matrix method. The standing optical field in the resonant cavity were also simulated in order to design the epitaxial structure for obtaining a optimal optical gain.

The fabrication steps of the two dielectric DBRs VCSELs are also demonstrated. Basic theory of the laser lift-off technique used in our work is reviewed and introduced. We have introduced a theory of the semiconductor microcavity and discussed the interaction between excitons and photons in the strong coupling regime. We also explore the Bose Einstein condensation characteristics. for polariton at the same time.

Chapter 3 shows the performance of the optically pumped GaN-based VCSELs. The threshold condition, cavity Q factor, characteristic temperature, polarization of the laser emission, divergent angle, gain and linewidth enhancement factor are characterized and discussed. The inhomogeneous indium composition in the InGaN/GaN MQWs are observed.

Chapter 4 present the frequency spacing between adjacent PL peaks decreases by almost a factor of five from 470 nm to 370 nm. We use the intrinsic material index dispersion and polariton dispersion to fit the experimental data, it shows that the latter fitting curve is much better than the former one. It is shown a very strong polariton dispersion in a multimode GaN surface emitting microcavity at room temperarure.

In the final chapter, chapter 5, an overview of this hesis and directions of future works are given and proposed.

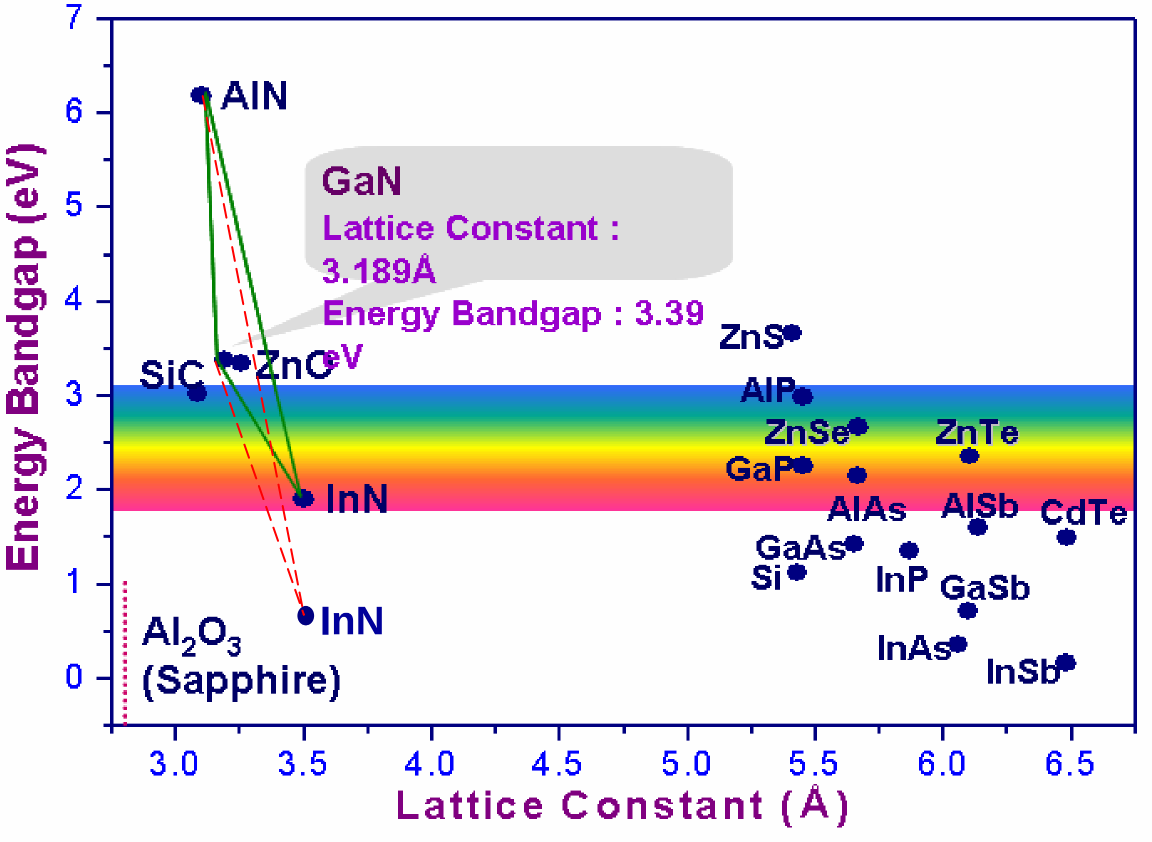

Figure 1.1 Lattice constant as s function of band gap energy of III-V nitride compounds.

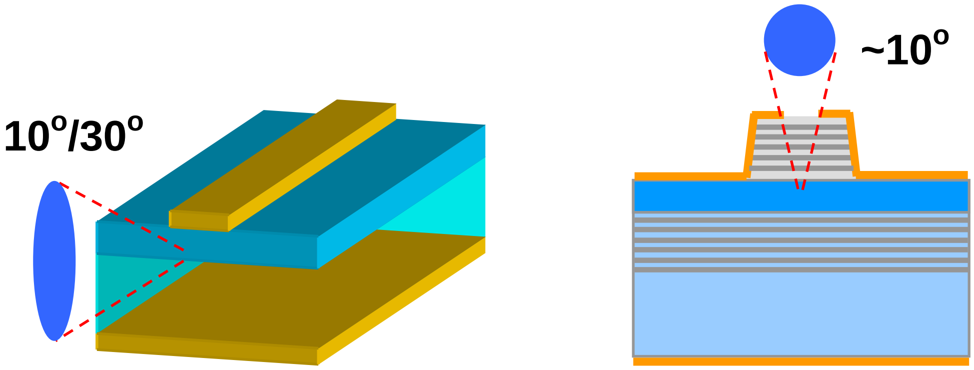

(a) (b)

Figure 1.2 (a) Schematic structure of EEL. (b) Schematic structure of VCSEL.

Reference

[1.1] S. Yoshida, S. Misawa and S. Gonda: Appl. Phys. Lett. **42**, 427 (1983)

[1.2] H. Amano, N. Sawaki, I. Akasaki and T. Toyoda: Appl. Phys. Lett. **48**, 353 (1986)

[1.3] S. Nakamura and G. Fasol: *The Blue Laser Diode* (Heidelberg: Springer,1997)

[1.4] S. Nakamura: Jpn. J. Appl. Phys. **30**, L1705 (1991)

[1.5] S. Strite and H. Morko: J. Vac. Sci. Technol. B **10**, 1237 (1992)

[1.6] F. A. Ponce and D. P. Bour: Nature **386**, 351 (1997)

[1.7] H. Amano, M. Kito, K. Hiramatsu and I. Akasaki: Japan. J. Appl. Phys. **28**, L2112 (1989)

[1.8] S. Nakamura, T. Mukai , M. Senoh and N. Iwasa: Japan. J. Appl. Phys. **31**, L139 (1992)

[1.9] S. Nakamura, N. Iwasa, M. Senoh and T. Mukai: Japan. J. Appl. Phys. **31**, 1258 (1992)

[1.10] S. Nakamura , T. Mukai, M. Senoh, S. Nagahama and N. Iwasa: J. Appl. Phys. **74**, 3911 (1993)

[1.11] S. Chichibu, T. Azuhata, T. Sota and S. Nakamura: Appl. Phys. Lett. **69**, 4188 (1996)

[1.12] S. Chichibu, T. Azuhata, T. Sota and S. Nakamura: Appl. Phys. Lett. **70**, 2822 (1997)

[1.13] Y. Narukawa, Y. Kawakami, Sz Fujita, Sg Fujita and S. Nakamura: Phys. Rev. B **55**, 1938 (1997)

[1.14] Y. Narukawa, Y. Kawakami, M. Funato, Sz Fujita, Sg Fujita and S. Nakamura: Appl. Phys. Lett. **70**, 981 (1997)

[1.15] S. Chichibu, K. Wada and S. Nakamura: Appl. Phys. Lett. **71**, 2346 (1997)

[1.16] C. Huh, K. S. Lee, E. J. Kang and S. J. Park: J. Appl. Phys. **93**, 9383 (2003)

[1.17] Compound Semiconductors 7(1), 7 (2001).

[1.18] W. S. Wong and T. Sands: Appl. Phys. Lett. **75**, 1036 (1999)

[1.19] J. J. Wierer, D. A. Steigerwald, M. R. Krames, J. J. O'Shea, M. J. Ludowise, G. Christenson, Y.-C. Shen, C. Lowery, P. S. Martin, S. Subramanya, W. Gotz, N. F. Gardner, R. S. Kern, and S. A. Stockman: Appl. Phys. Lett. **78**, 3379 (2001)

[1.20] J. Shakya, K. H. Kim, J. Y. Lin and H. X. Jiang: Appl. Phys. Lett. **85**, 142 (2004)

[1.21] H. Amano, T. Asahi and I. Akasaki: Jpn. J. Appl. Phys. 29, L205 (1990)

[1.22] A.S. Zubrilov, V.I. Nikolaev, D.V. Tsvetkov, V.A. Dmitriev, K.G. Irvine, J.A. Edmond and C.H. Carter: Appl. Phys. Lett. 67, 533 (1995)

[1.23] T. Someya, K. Tachibana, J. Lee, T. Kamiya, and Y. Arakawa: Jpn. J. Appl. Phys., vol. 37, pp. L1424-L1426, Dec. 1998.

[1.24] T. Someya, R. Werner, A. Forchel, M. Catalano, R. Cingolani, and Y. Arakawa: Science, vol. 285, pp. 1905-1906, Sep. 1999.

[1.25] M.A. Khan, S. Krishnankutty, R.A. Skogman, J.K. Kuznia and D.T. Olson: Appl, Phys. Lett. 65, 520 (1994).

[1.26] S.T. Kim, H. Amano and I. Akasaki: Appl. Phys. Lett. 67, 267 (1995).

[1.27] H. Amano, T. Tanaka, Y. Kunii, K. Kato, S.T. Kim and I. Akasaki: Appl. Phys. Lett. 64, 1377 (1994).

[1.28] R.L. Aggarwal, P.A. Maki, R.J. Molnar, Z.L. liau and I. Melngailis: J. Appl. Phys. 79, 2148 (1996).

[1.29] T.J. Schmidt, X.H. Yang, W. Shan, J.J. Song, A. Salvador, W. Kim, O. Aktas, A.

Botchkarev, and H. Morkoc: Appl. Phys. Lett. 68,1820 (1996).

[1.30] S. Nakamura, M. Senoh , S. Nagahama, N. Iwasa, T. amada, T. Masushita, H. Kiyoku and Y. Sugimoto: Jpn. J. Appl. Phys. **35**, L74 (1996)

[1.31] K. Itaya: Japan. J. Appl. Phys. **35**, L1315 (1996)

[1.32] G. E. Bulman, K. Doverspike , S. T. Sheppard, T. W. Weeks, H. S. Kong, H. M. Dieringer, J. A. Edmond, J. D. Brown, J. T. Swindell and J. F. Schetzena: Electron. Lett. **33**, 1556 (1997)

[1.33] M. P. Mack, A. Abare, m. Aizcorbe, P. Kozodoy, S. Keller, U. K. Mishra, L. Coldren and S. DenBaars: 1997 MRS Internet J. Nitride Semicond. Res. 2 41 (available from http://nsr.mij.mrs.org/2/41/)

[1.34] A. Kuramata, K. Domen, R. Soejima, K. Horino, S. Kubota and T. Tanahashi: Jpn. J. Appl. Phys. **36**, L1130 (1997)

[1.35] F. Nakamura et al 1998 J. Crystal Growth 189/190 84

[1.36] M. Kneissl, D. P. Bour, N. M. Johnson, L. T. Romano, B. S. Krusor, R. Donaldson, J. Walker and C. D. Dunnrowicz: Appl. Phys. Lett. **72**, 1539 (1998)

[1.37] H. Katoh, T. Takeuchi, C. Anbe, R. Mizumoto, S. Yamaguchi, C. Wetzel, H. Amano, I. Akasaki, Y. Kaneko and N. Yamada: Jpn. J. Appl. Phys. **37**. L 444 (1998)

[1.38] Nanfang Yu, Romain Blanchard, Jonathan Fan, Federico Capasso, Tadataka Edamura, Masamichi Yamanishi, and Hirofumi Kan: Appl. Phys. Lett. 93, 181101 (2008)

[1.39] S. Nakamura: Japan. J. Appl. Phys. **37**, L627 (1998)

[1.40] S. Nakamura: Japan. J. Appl. Phys. **37**, L309 (1998)

[1.41] T. Someya, R. Werner, A. Forchel, M. Catalano, R. Cingolani, and Y. Arakawa:

Science, vol. 285, pp. 1905-1906, Sep. 1999.

[1.42] Y. –K. Song, H. Zhou, M. Diagne, I. Ozden, A. Vertikov, A. V. Nurmikko, C. Carter-Coman, R. S. Kern, F. A. Kish, and M. R. Krames: Appl. Phys. Lett., vol. 74, pp. 3441-3443, Jun. 1999.

[1.43] H. Zhou, M. Diagne, E. Makarona, J. Han, K. E. Waldrip, and J. J. Figiel: Electron. Lett., vol. 36, pp. 1777-1779, Oct. 2000.

[1.44] Y. –K. Song, H. Zhou, M. Diagne, A. V. Nurmikko, R. P. Schneider, Jr., C. P. Kuo, M. R. Krames, R. S. Kern, C. Carter-Coman, and F. A. Kish: Appl. Phys. Lett., vol. 76, pp. 1662-1664, Mar. 2000.

[1.45] T. Tawara, H. Gotoh, T. Akasaka, N. Kobayashi, and T. Saitoh: Appl. Phys. Lett., vol. 83, pp. 830-832, Aug. 2003.

[1.46] E. Feltin, G. Christmann, J. Dorsaz, A. Castiglia, J. –F. Carlin, R. Butté, N. Grandjean, S. Christopoulos, G. Baldassarri Höger von Högersthal, A. J. D. Grundy, P. G. Lagoudakis, and J. J. Baumberg: Electron., Lett., vol. 43, pp. 924-925, Aug. 2007.

[1.47] A. Castiglia, D. Simeonov, H. J. Buehlmann, J. –F. Carlin, E. Feltin, J. Dorsaz, R. Butté, and N. Grandjean: Appl. Phys. Lett., vol. 90, pp. 033514/1-3, Jan. 2007.

[1.48] T. -C. Lu, C. -C. Kao, H. -C. Kuo, G. -S. Huang, and S. -C. Wang: Appl. Phys. Lett., vol. 92, pp. 141102/1-3, Apr. 2008.

[1.49] Y. Higuchi, K. Omae, H. Matsumura, and T. Mukai: Appl. Phys. Express., vol. 1, 121102/1-3, Dec. 2008

[1.50] J. M. Redwing, D. A. S. Loeber, N. G. Anderson, M. A. Tischler, and J. S. Flynn: Appl. Phys. Lett. **69**, 1 (1996)

[1.51] T. Someya, K. Tachibana, J. Lee, T. Kamiya, and Y. Arakawa: Jpn. J. Appl. Phys.

37, L1424 (1998)

[1.52] Y.-K. Song, H. Zhou, M. Diagne, I. Ozden, A. Vertikov, A. V. Nurmikko, C. Carter-Coman, R. S. Kern, F. A. Kish, and M. R. Krames: Appl. Phys. Lett. **74**, 3441 (1999)

[1.53] T. Someya, R.Werner, A. Forchel, M. Catalano, R. Cingolani and Y.Arakawa: Science, 285, 1905 (1999)

[1.54] T. Tawara, H. Gotoh, T. Akasaka, N. Kobayashi and T. Saitoh: Appl. Phys. Lett., 83, 830 (2003)

[1.55] Y.-K. Song, H. Zhou, M. Diagne, A. V. Nurmikko, R. P. Schneider, Jr., C. P. Kuo, M. R. Krames, R. S. Kern, C. Carter-Coman and F. A. Kish: Appl. Phys. Lett., 76, 1662 (2000)

[1.56] H. Zhou, M. Diagne, E. Makarona, A. V. Nurmikko, J. Han, K. E. Waldrip and J. J. Figiel: Electron. Lett., 36,1777 (2000)

[1.57] T. Someya, K. Tachibana, J. Lee, T, Kamiya and Y. Arakawa: Jpn. J. Appl. Phys., 37, L1424 (1998)

[1.58] J. M. Redwing, D. A. S. Loeber, N. G. Anderson, M. A. Tischler, and J. S. Flynn: Appl. Phys. Lett., 69, 1 (1996)

[1.59] S. H. Park, J. Kim, H. Jeon, T. Sakong, S. N. Lee, S. Chae, Y. Park, C. H. Jeong, G. Y. Yeom, and Y. H. Cho: Appl. Phys. Lett., 83, 2121 (2003)

[1.60] M. Pelton, C. Santori, J. Vuckovic, B. Zhang, G. S. Solomon, J. Plant, and Y. Yamamoto: Phys. Rev. Lett. **89**, 233602 (2002)

[1.61] H. Deng, G. Weihs, C. Santori, J. Bloch, and Y. Yamamoto: Science **298**, 199 (2002)

[1.62] T. Kobayashi, T. Segawa, A. Morimoto, and T. Sueta: presented at 43rd Fall Meet. Japan Society of Applied Physics, Tokyo, September, 1982

[1.63] M. S. Skolnick, T. A. Fisher, and D. M. Whittaker: Semicond. Sci. Technol., vol. 13, pp. 645-669, Mar. 1998.

[1.64] S. Christopoulos, G. Baldassarri Höger von Högersthal, A. J. D. Grundy, P. G. Lagoudakis, A. V. Kavokin, J. J. Baumberg, G. Christmann, R. Butté, E. Feltin, J. –F. Carlin, and N. Grandjean: Phys. Rev. Lett., vol. 98, pp. 126405/1-4, Mar. 2007.

[1.65] G. Christmann, R. Butté, E. Feltin, J. –F. Carlin, and N. Grandjean: Appl. Phys. Lett., vol. 93, pp. 051102/1-3, Aug. 2008.

Chapter 2

Fundamental of GaN-based vertical cavity surface emitting lasers and semiconductor microcavities

2.1 Vertical cavity surface emitting lasers

2.1.1 Fundamental of VCSELs

As depicted in Figure 2.1, the typical structure of most VCSELs consist of two parallel reflectors which are distributed Bragg reflectors (DBRs), and a cavity including a multiple quantum wells (MQWs) served as active layer. Besides, diode lasers like the other types of lasers, diode laser contain three ingredients, including Gain medium, pumping source, and resonant cavity. The gain medium consists of a material which normally absorbs incident radiation over some wavelength range of interest. But, if it is pumped by inputting either electrical or optical energy, the electrons within the material can be excited to the higher, nonequilibrium energy level, so that the incident radiation can be amplified rather than absorbed by stimulating the de-excitation of these electrons along with the generation of additional radiation. If the resulting gain is sufficient to overcome the losses of some resonant optical mode of the cavity, this mode is said to have reached threshold, and relatively coherent light will be emitted. Pumping source provides the energy that can excite the electrons within gain medium at lower energy level to higher energy level. It could be either optical or electrical energy. The resonant cavity provides the necessary positive feedback for the radiation being amplified, so that a lasing oscillation can be established and sustained above threshold pumping level. Therefore, the reflectivity necessary to reach the lasing threshold should normally be higher than 99.9%. Corresponding to the ingredients of a laser, the active layer is the gain medium that amplify the optical radiation in the cavity; the top DBR, bottom DBRs and cavity form a resonant cavity where the radiation can interact with active region and have positive feedback.

An optical cavity or optical resonator is an arrangement of mirrors that forms a standing wave cavity resonator for light waves. Light confined in the cavity reflect multiple times producing standing waves for certain resonance frequencies. The standing wave patterns produced are called modes; longitudinal modes differ only in frequency while transverse modes differ for different frequencies and have different intensity patterns across the cross section of the beam. Recently, the Fabry-Perot cavity are employed in nearly all laser cavity. It is by using the interference of light reflected many times between two coplanar lightly-silvered mirrors. It is a high resolution instrument that has been used today in precision measurement and wavelength comparisons in spectroscopy. Also, the Fabry-Perot cavities can be used to ensure precise tuning of laser frequency. The thickness of the cavity and the position of the MQWs inside the MCs are two key features of the VCSEL devices. Thickness of a cavity decides the resonant wavelength that will lase above threshold condition according to $L = N\frac{\lambda}{2n}$, where L is cavity length, N is an integral, λ is resonant wavelength and n is the refractive index of the cavity. Usually the resonant wavelength of the cavity is chosen to be equal to the Bragg wavelength, such that the resonant wavelength can encounter the maximum reflectivity of the DBR. Typically, the cavity length of VCSELs is on the order of few half operating wavelengths. In such a short cavity device, the electromagnetic waves would form standing wave patterns with nodes (electromagnetic wave intensity minima) and anti-nodes (electromagnetic wave intensity maxima) within the GaN microcavity. The location of the InGaN/GaN MQWs with respect to the anti-modes can significantly affect the coupling of laser mode with the cavity field. As the MQWs are well aligned with the cavity field, the more electromagnetic wave interact with the MQWs result in more photon generated in the cavity, that is optical gain of resonant mode is increased. The proper alignment of the MQWs region with the anti-nodes of the cavity standing wave field patterns will enhance the coupling and reduce laser threshold condition. As a result, the precise layer thickness control in the VCSEL fabrication is important. Therefore, optical cavities are designed to have a large Q factor; a beam will reflect a very large number of times with little attenuation and the frequency linewidth of the beam is very small indeed compared to the frequency of the laser.

2.1.2 Distributed Bragg reflector

In the GaN-based VCSEL structure, a micro cavity with a few λ in the optical thickness and a pair of high reflectivity (above 99%) distributed Bragg reflectors (DBRs) are necessary for reducing the lasing threshold. Recently, several groups have reported optically pumped GaN-based VCSELs mainly using three different kinds of vertical resonant cavity structure forms: (1) monolithically grown vertical resonant cavity consisting of epitaxially grown III-nitride top and bottom DBRs (epitaxial DBR VCSEL), (2) vertical resonant cavity consisting of dielectric top and bottom DBR (dielectric DBR VCSEL). (3) vertical resonant cavity consists of an epitaxially grown III-nitride top DBR and a dielectric DBR (hybrid DBR VCSEL).

In order to obtain high reflectivity DBRs to reduce the threshold condition of the

VCSELs, dielectric DBRs was used in the GaN-based VCSEL in this study. Distributed Bragg reflector (DBR) consists of an alternating sequence of high and low refractive index layers with quarter-wavelength thickness, as Figure 2.2 [2.1]. Therefore, it's necessary to know the theory of quarter-wave layer before discussing the DBRs. Now, consider the simple case of a transparent plate of dielectric material having a thickness d and refractive index n_f, as shown in Figure 2.3. Suppose that the film is nonabsorbing and that the amplitude-reflection coefficients at the interfaces are so low that only the first two reflected beams (both having undergone only one reflection) need be considered. The reflected rays are parallel on leaving the film and will interference at image plane. The optical path difference (P) for the first two reflected beam is given by

$$P = n_f[(\overline{AB}) + (\overline{BC})] - n_1(\overline{AD}) \tag{2.1}$$

And since

$$\left(\overline{AB}\right) = \left(\overline{BC}\right) = \frac{d}{\cos\theta_t} \tag{2.2}$$

$$\left(\overline{AD}\right) = \left(\overline{AC}\right)\sin\theta_i \tag{2.3}$$

Using Snell's Law

$$n_1 \sin\theta_i = n_f \sin\theta_t \tag{2.4}$$

Then

$$\left(\overline{AD}\right) = \left(\overline{AC}\right)\frac{n_f}{n_1}\sin\theta_t \tag{2.5}$$

also

$$\left(\overline{AD}\right) = 2d\tan\theta_t \tag{2.6}$$

The eq. (2.1) becomes

$$P = \frac{2n_f d}{\cos\theta_t}(1 - \sin^2\theta_t) = 2n_f d\cos\theta_t \tag{2.7}$$

The corresponding phase difference (δ) associated with the optical path length difference is then just the product of the free-space propagation number and P, that is, K_0P. If the film is immersed in a single medium, the index of refraction can simply be written as $n_1=n_2=n$. It is noted that no matter n_f is greater or smaller than n, there will be a relative phase shift π radians.

Therefore, $$d\cos\theta_t = \frac{(2m+1)\lambda_0}{4} \qquad (m=0,1,2,3,\ldots) \qquad (2.8)$$

$$\delta = \frac{4\pi n_f (n_f^2 - n^2 \sin^2\theta_i)^2}{\lambda_0} \pm \pi \qquad (2.9)$$

The interference maximum of reflected light is established when $\delta=2m\pi$, in other words, an even multiple of π. In that case, eq. (2.8) can be rearranged; and the interference minimum of reflected light when $\delta = (2m\pm1)\pi$, in other words, an odd multiple of π. In that case eq. (2.9) also can be rearranged.

$$\begin{cases} d\cos\theta_t = \dfrac{(2m+1)\lambda_0}{4n_f}, (m=0,1,2,3,\ldots) & [\max imum] \\ d\cos\theta_t = \dfrac{2m\lambda_0}{4n_f}, (m=0,1,2,3,\ldots) & [\min imum] \end{cases} \qquad (2.10)$$

Therefore, for an normal incident light into thin film, the interference maximum of reflected light is established when $d = \lambda_0/4n_f$ (at m=0). Based on the theory, a periodic structure of alternately high and low index quarter-wave layer is useful to be a good reflecting mirror. This periodic structure is also called Distributed Bragg Reflectors (DBRs). Therefore, the concept of DBR is that many small reflections at the interface between two layers can add up to a large net reflection. At the Bragg frequency the reflections from each discontinuity add up exactly in phase. Spectral-dependent of the reflectivity can be calculated by the transfer-matrix method [2.2]. Considering a layer if dielectric material *b* which is clad between two layers *a* and *c*. A transverse electromagnetic wave at normal incidence propagates throught the layer in *z* direction.

Taking the electric and magnetic (E and H) fields into consideration by Maxwell's equation, a transmission matrix relating these fields can be written as

$$\begin{pmatrix} E(0) \\ \eta_0 H(0) \end{pmatrix} = \begin{pmatrix} \cos(k_b d) & \frac{j}{n_b}\sin(k_b d) \\ j n_b \sin(k_b d) & \cos(k_b d) \end{pmatrix} \begin{pmatrix} E(d) \\ \eta_0 H(0) \end{pmatrix} \tag{2.11}$$

In the equation, n_b is the refractive index of layer b and η_o the impedance of free space, j is the unit imaginary number, k_b is the phase propagation constant in layer b, $k_b = \frac{2\pi}{n_b \lambda}$, where λ is the wavelength in free space. Here, the absorption was not considered in this discussion. For a multilayer, a matrix M_i is formed for each layer i of thickness d_i in the stack. By considering the effect of all layers with summation length of each layers L, a matrix M relates to input and output fields ca be obtained,

$$\begin{cases} \begin{pmatrix} E(0) \\ H(0) \end{pmatrix} = M \begin{pmatrix} E(L) \\ H(L) \end{pmatrix} \\ M = \prod_i M_i = \begin{pmatrix} m_{11} & m_{12} \\ m_{21} & m_{22} \end{pmatrix} \end{cases} \tag{2.12}$$

The reflection coefficient r of the stack is:

$$r = \frac{Y_0 m_{11} + Y_0 m_{12} - m_{21} - Y_s m_{22}}{Y_0 m_{11} + Y_0 m_{12} + m_{21} + Y_s m_{22}} \tag{2.13}$$

where the Y is wave admittance and o and s refer to the incident and substrate respectively. If we have a layer of index n_l between layer o and s of lower under, then the reflection from interface has a phase of π radians relative to the incident wave, because of the positive index step. If the thickness of the layer is a quarter wavelength the two reflection add in phase at the front interface due to the π round trip phase delay for the second reflection. For a stack with many alternate 1/4 wave (or (n/2+1/4) wave, *n* integral) layers of low and high index, all interfacial reflections will add in phase.

For a Bragg reflector made from quarter wavelength layers of indices n_1 and n_2,as shown in Figure 2.4, the maximum reflectivity R at resonant wavelength, also denoted as Bragg wavelength (λ_B), of a stack with m non-absorbing pairs can be expressed by:

$$R = \left[\frac{1 - \frac{n_s}{n_0}(\frac{n_1}{n_2})^{2m}}{1 + \frac{n_s}{n_0}(\frac{n_1}{n_2})^{2m}} \right]^2 \qquad (2.14)$$

The n_o and n_s in the equation are the refractive indices of incident medium and substrate, respectively and *m* is pair numbers of the DBR. Layer thicknesses $L_{1,2}$ have to be chosen as $L_{1,2}=\lambda_B\ /(4n_{1,2})$. The maximum reflectivity of a DBR therefore increases as the increasing difference in refractive indices and pair number of DBR. A broad spectral plateau of high reflectivity, denoted as a stop-band, appear around the Bragg wavelength, the width of which can be estimate as [2.3] $\Delta\lambda_{sb} \approx \frac{2\lambda_B \Delta n}{\pi n_{eff}}$. A wide stop-band provides a larger tolerance between the designed λ_B and the main wavelength of the cooperated MQWs, this is another important reason for us to use dielectric DBRs as mirrors in our VCSEL structure. When two such high-reflectance DBRs are attached to a layer with an optical thickness integer times of $\lambda_c / 2$ $(\lambda_c \approx \lambda)$, a cavity resonance is formed at λ_c, leading to a sharp increase of the transmission *T* at λ_c:

$$T = \frac{(1-R_1)(1-R_2)}{[1-\sqrt{R_1 R_2}]^2 + 4\sqrt{R_1 R_2}\sin^2(\frac{\phi}{2})} \qquad (2.15)$$

where ϕ is the cavity round-trip phase shift of a photon at λ_c.

If $(R_1 \approx R_2 = R), (\frac{1-R}{2})^2 \le T \le 1$ depending on ϕ. One characteristic parameter of the cavity quality is the cavity quality factor Q defines as:

$$Q = \frac{\lambda_c}{\Delta\lambda_c} \approx \frac{\pi(R_1R_2)^{1/4}}{1/(R_1R_2)^{1/2}} \tag{2.16}$$

Where $\Delta\lambda_c$ is the width of the resonance. An ideal cavity has $Q = \infty$. If the cavity length is $\lambda/2$, Q is the average number of round trips a photon travels inside the cavity before it escapes. Figure 2.5 shows an example of the reflection spectrum of a cavity.

The high-reflectivity or stop band of a DBR depends on the difference in refractive index of the two constituent materials, △n (≡n_1-n_2). We can calculate by requiring the same optical path length normal to the layers for the DBR and the effective medium. The effective refractive index is then given by

$$n_{eff} = 2\left(\frac{1}{n_1} + \frac{1}{n_2}\right)^{-1} \tag{2.17}$$

For DBRs, the optical wave penetrates into the reflector by one or several quarter-wave pairs. Only a finite number out of the total number of quarter-wave pairs are effective in reflecting the optical wave. The effective number of pairs seen by the wave electric field is given by

$$m_{eff} = \frac{1}{2}\frac{n_1 + n_2}{n_1 - n_2}\tanh\left(2m\frac{n_1 - n_2}{n_1 + n_2}\right) \tag{2.18}$$

For very thick DBRs (m→∞) the tanh function approaches unity and one obtains

$$m_{eff} \approx \frac{1}{2}\frac{n_1 + n_2}{n_1 - n_2} \tag{2.19}$$

Also, the penetration depth is given by

$$L_{pen} = \frac{L_1 + L_2}{4r}\tanh(2mr) \qquad (2.20)$$

where r = $(n_1-n_2)/(n_1+n_2)$ is the amplitude reflection coefficient.

For a large number of pairs (m→∞), the penetration depth is given by

$$L_{pec} \approx \frac{L_1 + L_2}{4r} = \frac{L_1 + L_2}{4}\frac{n_1 + n_2}{n_1 - n_2} \qquad (2.21)$$

Comparison of eqs. (2.17) and (2.19)

$$L_{pen} = \frac{1}{2} m_{eff} (L_1 + L_2) \qquad (2.22)$$

The factor of (1/2) in Eq. (2.20) is due to the fact that m_{eff} applies to effective number of periods seen by the electric field whereas L_{pen} applies to the optical power. The optical power is equal to the square of the electric field and hence it penetrates half as far into the mirror. The effective length of a cavity consisting of two DBRs is thus given by the sum of the thickness of the center region plus the two penetration depths into the DBRs. So effective cavity length is extended in a semiconductor microcavity as $L_{eff} = L_c + L_{DBR}$

2.2 Fundamental of semiconductor microcavities

2.2.1 polariton dispersion curve in the strong coupling regime

A typical structure of a semiconductor microcavity consisting of a $\lambda/2$ cavity layer sandwiched between two DBRs. The planar semiconductor MCs in the strong coupling regime have attracted a good deal of attention and controlled the interaction between photons and excitons, which leads to cavity polaritons, as shown in Figure 2.6. When the exciton state is strongly coupled to the cavity-photon mode, quasi-particle called cavity polaritons are produced with an anti-crossing dispersion relation, as shown in Figure 2.7.

Thus, the elementary excitations of the system are no longer exciton or photon, but a new type of quasi-particle called the polaritons. Polaritons, predicted theoretically by Hopfield [2.4] and Agranovich [2.5] in the end of 1950s, have been extensively studied in bulk semiconductor materials [2.6, 2.7], thin films [2.8, 2.9], quantum wells [2.10, 2.11], and quantum wires and dots [2.12, 2.13]. They can be interpreted as virtual exciton–photon pairs that propagate in the crystal because of a chain of processes of virtual absorption and emission of photons by excitons. The polariton states are true eigenstates of the system, so that once the polaritons are present there are no more pure excitons or photons. The exciton-photon interaction are often described by linear dielectric dispersion model [2.14] or coupled oscillator model [2.15]. The dielectric dispersion is used to described transmissive or reflective spectral experiments. The coupled oscillator model on the other hand is more suitable for describing active PL experiment. In linear regime, the coupled oscillator rate equations for the interaction between a cavity mode a and exciton J are

$$\frac{da}{dt} = -\gamma_a a - i\omega a + igJ \tag{2.23}$$

$$\frac{dJ}{dt} = -\gamma_J J - i\Omega J + iga \tag{2.24}$$

where ω and Ω are photon and exciton frequencies, a and J are the respective decay rates, and g is the interaction constant. The formal solutions of polariton frequencies are

$\omega_{ex,\pm} = (\Omega + \omega)/2 - i(\gamma_J + \gamma_a)/2 \pm \sqrt{((\Omega - \omega) - i(\gamma_J - \gamma_a))^2 + 4g^2}/2$, where ± corresponds to the upper and lower branch polariton. We start from the Hamiltonian with the spacial dependence explicitly spelled out,

$$
\begin{aligned}
H &= H_{photon} + H_{exciton} + H_{\text{int.}} \\
&= \hbar\omega_n \sum_n a^+_{k_n} a_{k_n} + \int_x \hbar\Omega J^+(x)J(x) + i\hbar\sum_n g\int_x (a^+_{k_n} u^*_{k_n}(x)J(x) - J^+(x)a_{k_n}u_{k_n}(x))
\end{aligned}
\tag{2.25}
$$

where u_{kn}(x) is cavity mode function, k_n is the corresponding wave number, and J(x) is exciton field operator. We will discuss the spacial dependence of J(x) and exciton Hamiltonian in more detail shortly. The interaction of photon and exciton with reservoir are neglected for simplicity. These interactions introduce decay to photon and exciton and will be discuss later. g is the exciton-photon interaction constant. Excitons are treated as bosons under low excitation limit [2.16-18]. In the above exciton-photon interaction Hamiltonian H_{int}, the overlap integral projects exciton field on cavity modes u_{kn}. It can be shown that, using tight-binding model for exciton wave function, the exciton field in interaction with radiation behaves exactly as a quantized polarization field [2.17]. Similar result could also be obtained from using weak-binding model [2.17]. In our microcavity, excitons in GaN expand the whole cavity defined by two DBR mirrors. Applying the same cavity boundary condition to quantize exciton field, the exciton field is then written in terms of the same cavity mode functions as

$$
J(x) = \sum_n J_{k_n} u_{k_n}(x) \tag{2.26}
$$

where J_{k_n} is the exciton amplitude operator of mode function u_{kn} and satisfies the commutation relation $[J_{k_n}, J^+_{k_n'}] = \delta_{k_n k_n'}$. The use of cavity mode functions as a basis for exciton field to describe the exciton-photon interaction can be understood from another point of view. To be in the strong interaction regime, one would like to have a maximum overlap integral between the exciton field and cavity mode. This occurs for those excitons with the same cavity mode functions. Therefore, as far as cavity polariton is concerned, it is natural to express exciton field in terms of cavity mode functions.

From cavity boundary condition, the cavity mode function u_{kn} satisfies orthogonal relation $\int_x u^*_{k_n} u_{k_m} = \delta_{nm}$. Using this expression, the exciton Hamiltonian is rewritten as $\sum_n \hbar\Omega_n J^+_{k_n} J_{k_n}$, where Ω_n is the transition frequency of exciton mode n. Strictly speaking, the exciton transition frequency is wave vector dependent and expression Ω_n should be used. Here, we will treat it as a constant and drop index n from now on since the change of Ω_n is small within the range of cavity modes of interest. The Hamiltonian is thus simplified to

$$H = \hbar\omega_n \sum_n a^+_{k_n} a_{k_n} + \hbar\Omega \sum_n J^+_{k_n} J_{k_n} + i\hbar \sum_n g(a^+_{k_n} J_{k_n} - J^+_{k_n} a_{k_n}) \tag{2.27}$$

The formal operator rate equations are readily obtained as

$$\frac{da_{k_n}}{dt} = -i\omega_n a_{k_n} + igJ_{k_n} \tag{2.28}$$

$$\frac{dJ_{k_n}}{dt} = -i\Omega J_{k_n} + iga_{k_n} \tag{2.29}$$

One can see that each cavity mode is only coupled to the corresponding exciton mode. There are multiple independent cavity polaritons. The root cause of no cross coupling lies in the fact that mode functions u_{kn} are orthogonal and both photon and exciton fields are based on the same mode functions. The polariton frequencies for mode u_{kn} are

$$\omega_{pol,\pm} = (\Omega + \omega_n)/2 \pm \sqrt{(\Omega - \omega_n)^2 + 4g^2}\,/2 \tag{2.30}$$

Where ± is for upper/lower branch polariton.

In particular, the strength of exciton–light coupling is greatly enhanced in microcavities, which results in the so-called strong-coupling regime manifested by anti-crossing of the exciton–polariton modes, observed for the first time by ClaudeWeisbuch et al. [2.19] in 1992. These eigenmodes appeared to be split at the anti-crossing point that defines the strong-coupling regime. Splitting between modes at this point is widely referred to as vacuum-field Rabi splitting or simply Rabi splitting. In the opposite case of the weak-coupling regime, there is no splitting between polariton eigenmodes at the crossing point. The weak-coupling regime is realised, in particular, in VCSELs and vertical cavity light emitting diodes (VCLEDs). For a system of two oscillators there are two possibilities: either they continue to oscillate with the same frequency, or the system starts with two new eigenfrequencies split by a value proportional to the coupling strength between the two oscillators, as shown in Figure 2.7. The first regime is called the weak-coupling regime, and the second is called the strong-coupling regime. If there is no attenuation (appearance of non-zero imaginary parts of the eigenfrequencies) in the system, it is always in the strong-coupling regime. Also, magnetic field can increase the exciton oscillator strength and make it into the strong coupling regime. Note that in semiconductor MCs, strong coupling is usually invisible at room temperarure due to the exciton broadening altered by varying the temperature. Polariton dispersion curves is strongly dependent on the detuning between the bare cavity mode $\omega_c(k)$and the bare exciton mode $\omega_{ex}(k)$ at zero in-plane wave-vector $k=0$. The detuning δ is given by $\omega_c(0)$- $\omega_{ex}(0)$. Figure 2.8 shows three typical dispersion curves of cavity polaritons for positive, zero and negative detunings. One can see that at small k the dispersion of exciton–polaritons in the cavity is essentially parabolic, and can be characterised by some effective mass, while this mass varies dramatically as a function of detuning. The possibility of tuning the polariton effective mass over a wide range is an important peculiarity of microcavities. Recently, the observed Rabi splittings have reached 50 meV and 56 meV for 3λ/2 and 3λ cavity respectively [2.20, 2.21].

2.2.2 Bose Einstein condensation

Bose Einstein condensation (BEC) [2.22] has been a source of imagination and innovation of physicists ever since its first proposal by Einstein in 1925. The theory mainly focus on describing the characteristics of eigenstates distribution for Bosons, and the most appealing property is that bosons can coexist on the same energy level. In addition, the lower the energy level, the more the particle occupancym, it is far from fermion obeyed "Pauli exclusion principle". A BEC is a state of matter of a dilute gas of weakly interacting bosons confined in an external potential and cooled to temperatures very near to absolute zero . Under such conditions, a large fraction of the bosons collapse into the lowest quantum state of the external potential, and all wave functions overlap with each other, then quantum effects become apparent in a macroscopic scale. The first application of BEC to a physical system was by London in 1938 [2.23], right after the discovery of superfluid in liquid helium [2.24]. Though we can observe BEC by the characteristics of superfluid, we can not reach the same phenomena at room temperature It has attracted much attention owing to the polariton splitting phenomena of a planar GaAs microcavity discovered by C. Weisbush et al. and M, Nishioka et al. in 1992. In recent years, much attention has been given to the behavior of these cavity polaritons which is the so-called bosonic particles in the strong coupling regime. One area of interest relates to the BEC of cavity polaritons. These polaritons will condense to their final state with a gain as a result of certain scattering processes, and then coherent light will be emitted from the polaritons in that state. The BEC of the polaritons is expected to yield new scientific fields, such as the coherent manipulation of bosons in a solid state, and be applied to a new generation of devices, such as polariton lasers [2.25], polariton LED [2.26], and polariton amplification [2.27] without threshold or population inversion .

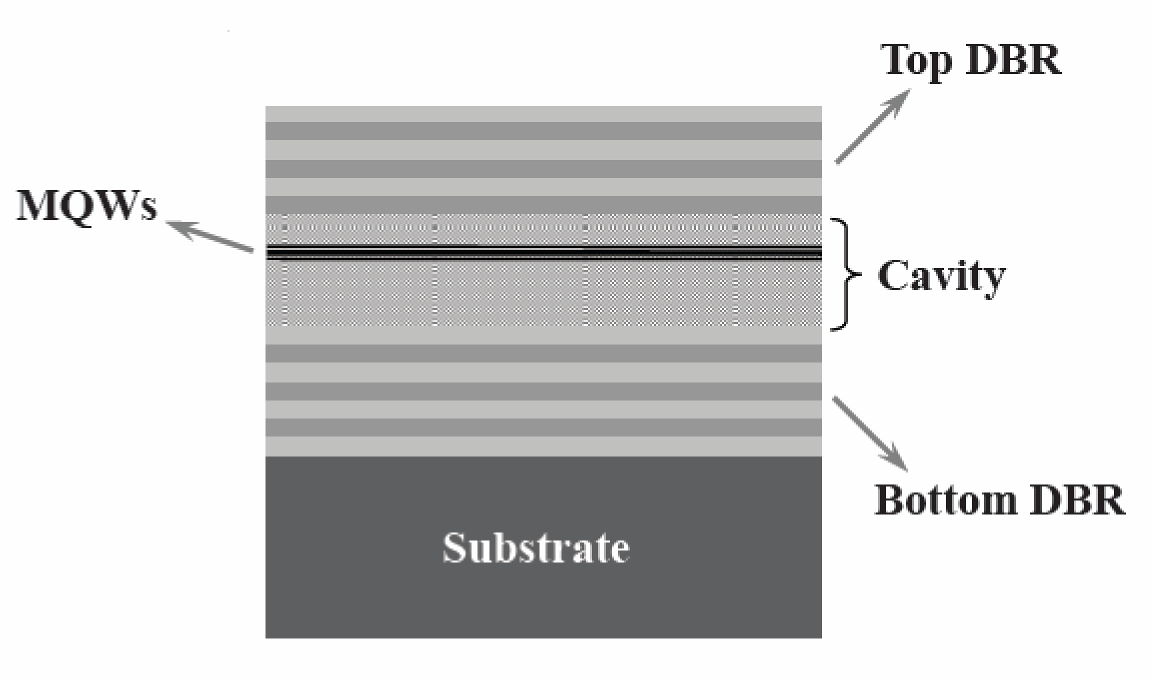

Figure 2.1 Basic geometry of a vertical cavity surface emitting laser.

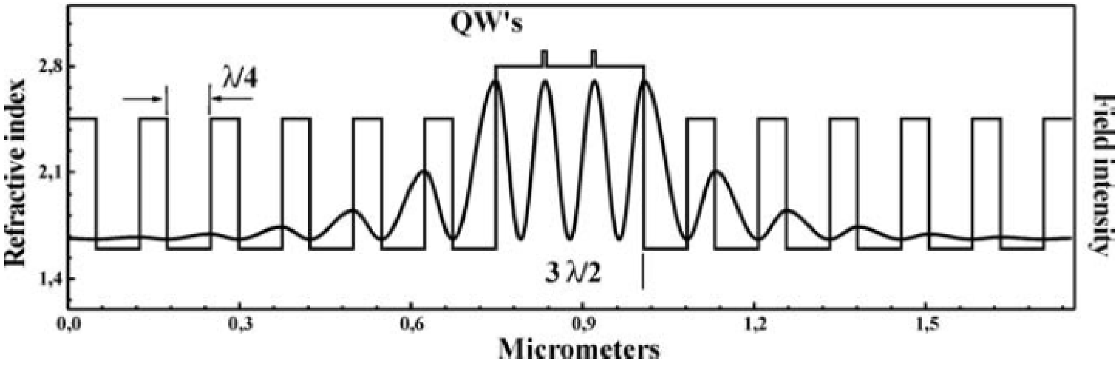

Figure 2.2 A typical microcavity structure. The central cavity layer having a thickness equal to an integer number of half-wave-lengths of light at the exciton resonance frequency is sandwiched between two Bragg mirrors. A quantum well (several quantum wells) should be embedded in the antinodes of the cavity mode electric field in order to provide the strongest coupling to light.

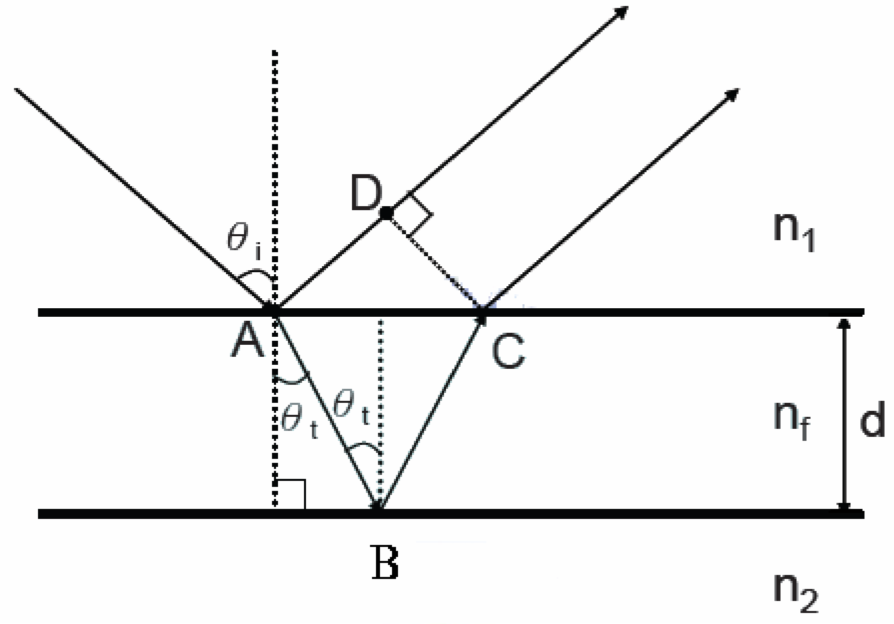

Figure 2.3 Schematic draw of the light reflected from the top and bottom of the thin film.

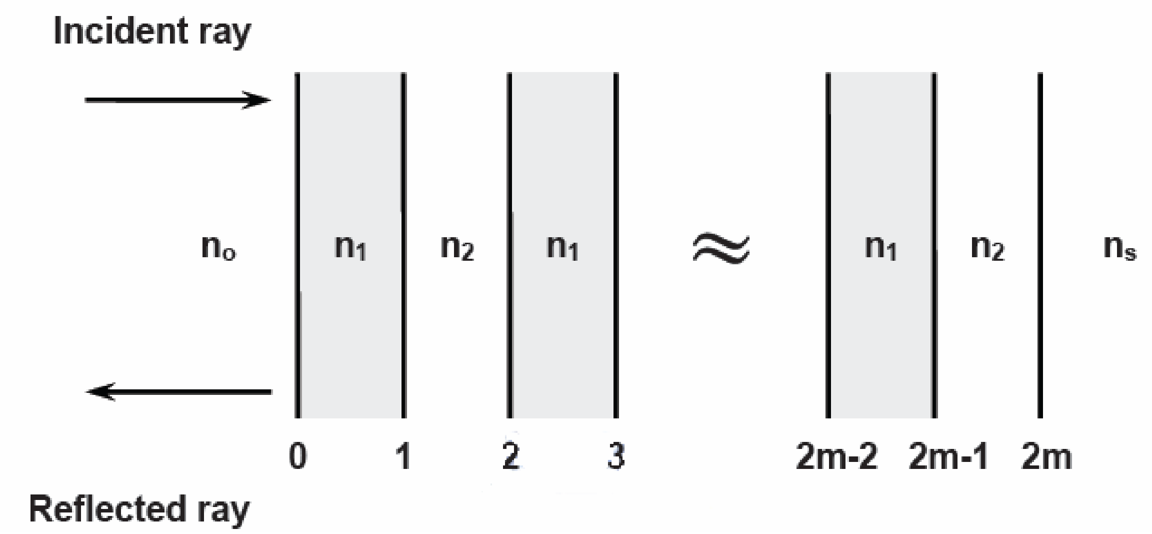

Figure 2.4 Schematic of distributed Bragg reflector incorporating m pairs of two mediums with indices n_1 and n_2.

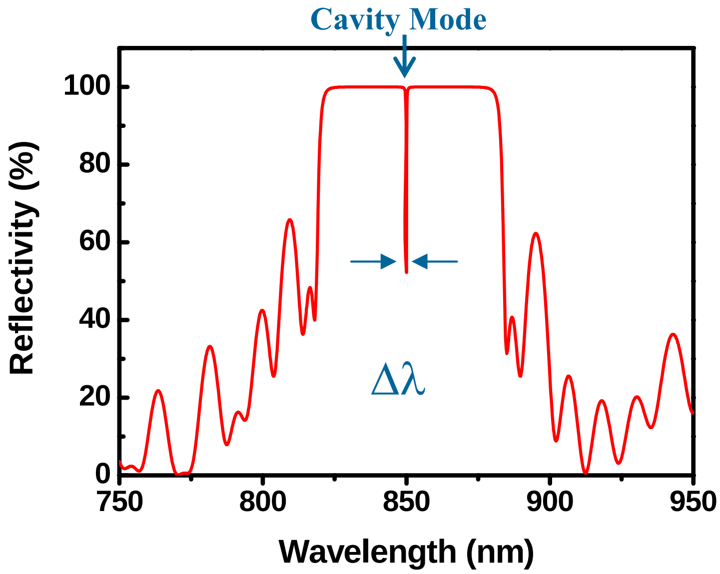

Figure 2.5 Reflectance of an $\lambda/2$ empty microcavity.

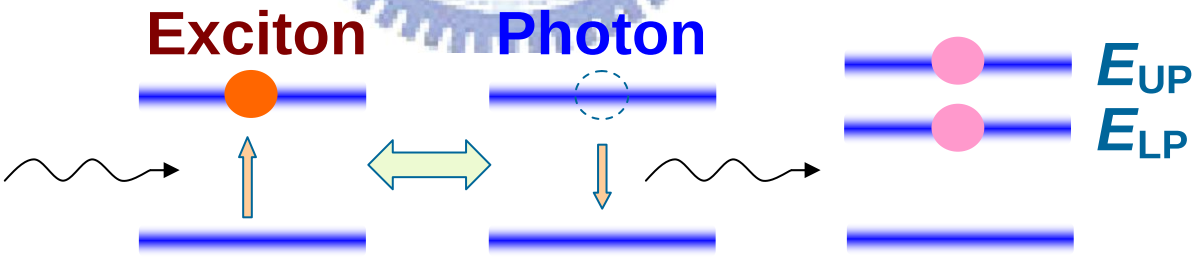

Figure 2.6 Polaritons are produced by interaction between excitons and photons.

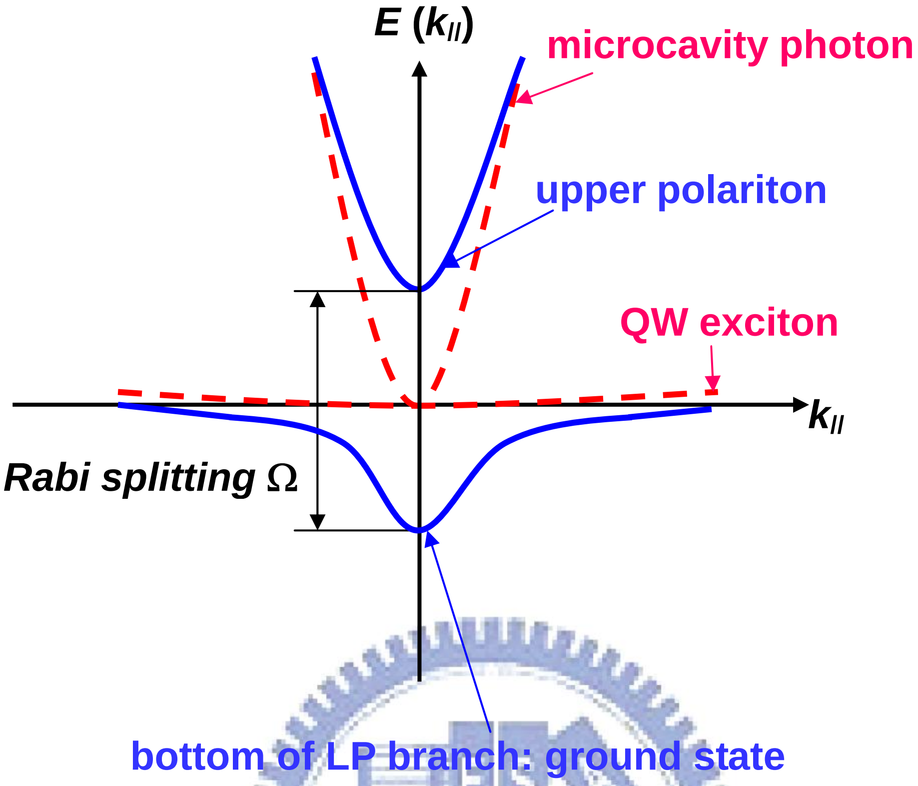

Figure 2.7 When the exciton state is strongly coupled to the cavity-photon mode, quasi-particle called cavity polaritons are produced with an anti-crossing dispersion relation.

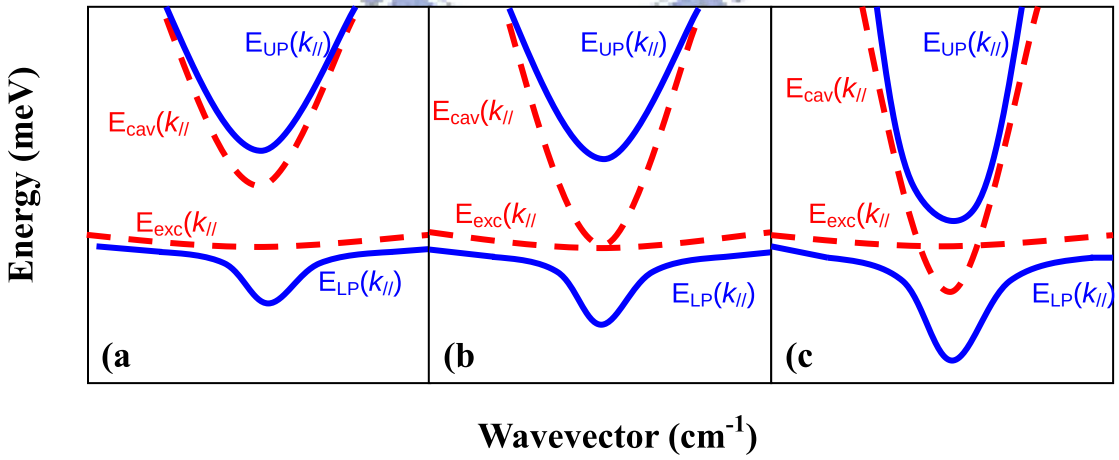

Figure 2.8 Polariton dispersion for different detuning between exciton and photon modes: (a) δ= positive, (b) δ= zero, (c) δ= negative. Dashed lines show the energies of uncoupled exciton and photon modes.

Reference

[2.1] Alexey Kavokin, Guillaume Malpuech: *Thin films and nanostructures: cavity polaritons*.

[2.2] T. E. Sale: *VERTICAL CAVITY SURFACE EMITTING LASERS*, (Research Studies Press LTD. 1995)

[2.3] Carl W. Wilmsen, Henryk Temkin and Larry A. Coldren: *Vertical-Cavity Surface-Emitting Lasers: Design, Fabrication, Characterization, and Applications*, (Cambridge, 1999)

[2.4] J. J. Hopfield, Theory of the contribution of excitons to the complex dielectric constant of crystals: Phys. Rev. 112, 1555 (1958).

[2.5]. V. M. Agranovich, Zh. Eksper. Teoret. Fiz. 37, 1555 (1959).

[2.6] V. M. Agranovich, V. L. Ginzburg: Interscience Publ., London, 1966.

[2.7] E. L. Ivchenko, Spatial dispersion effects in exciton resonance region, in “Excitons” (E. I. Rashba and M. D. Sturge, Eds.). Elsevier, North-Holland, 1982.

[2.8] D. Frölich, A. Kulik, B. Uebbing, A. Mysyrowicz, V. Langer, H. Stolz, W. von der Osten, Coherent propagation and quantum beats of quadrupole polaritons in Cu2O: Phys. Rev. Lett. 67, 2343 (1991).

[2.9]. G. Panzarini, L. C. Andreani, Bulk polariton beatings and two-dimensional radiative decay: Analysis of time-resolved transmission through a dispersive film: Solid State Comm. 102, 505 (1997).

[2.10] L. C. Andreani, F. Tassone, F. Bassani, Radiative lifetime of free excitons in quantum wells: Solid State Comm. 77, 641 (1991).

[2.11] E. L. Ivchenko, Excitonic polaritons in periodic quantum well structures: Sov. Phys. Solid State 33, 1344 (1991).

[2.12] E. L. Ivchenko, A. V. Kavokin, Light reflection from quantum well, quantum wire and quantum dot structures: Sov. Phys. Solid State 34, 1815 (1992).

[2.13] A. D'Andrea, R. Del Sole, Excitons in semiconductor confined systems: Solid State Comm. 74, 1121 (1990).

[2.14] A. P. D. Love, D. N. Krizhanovskii, D. M. Whittaker, R. Bouchekioua, D. Sanvitto, S. Al Rizeiqi, R. Bradley, M. S. Skolnick, P. R. Eastham, R. Andre, et al.: Phys. Rev. Lett. **101** (2008).

[2.15] T. Tawara, H. Gotoh, T. Akasaka, N. Kobayashi, and T. Saitoh: Phys. Rev. Lett. **92**, 256402 (2004).

[2.16] L. C. Andreani, G. Panzarini, and J.-M. G´erard: Phys. Rev. B **60**, 13276 (1999).

[2.17] J. J. Hopfield: Phys. Rev. **112**, 1555 (1958).

[2.18] S. Pau, G. Bj¨ork, J. Jacobson, H. Cao, and Y. Yamamoto: Phys. Rev. B **51**, 14437 (1995).

[2.19]. C. Weisbuch, M. Nishioka, A. Ishikawa, Y. Arakawa, Observation of coupled exciton–photon mode splitting in a semiconductor quantum microcavity: Phys. Rev. Lett. 69, 3314 (1992).

[2.20] J. Kasprzak, D. D. slonyshkov, R. Andre, L. S. Dang, and G. Malpuech: Phys. Rev. Lett. **101**, 146404 (2008).

[2.21] L. C. Andreani, G. Panzarini, and J.-M. G´erard: Phys. Rev. B **60**, 13276 (1999).

[2.22] Hui Deng: *DYNAMIC CONDENSATION OF SEMICONDUCTOR MICROCAVITY POLARITONS* (2006).

[2.23] London, F. The ¸-phenomenon of liquid helium and the Bose-Einstein degeneracy: *Nature* 141, 643 (1938).

[2.24] Allen, J. & Misener, A. Flow of liquid helium ii: *Nature* 141, 75 (1938).

[2.25] S. Christopoulos, G. Baldassarri Ho¨ger von Ho¨gersthal, A. J. D. Grundy, P. G. Lagoudakis, A.V. Kavokin, and J. J. Baumberg G. Christmann, R. Butte´, E. Feltin, J.-F. Carlin, and N. Grandjean: Phys. R. Lett. 98 126405 (2007).

[2.26] S. I. Tsintzos, N. T. Pelekanos, G. Konstantinidis, Z. Hatzopoulos,and P. G. Savvidis : Nature 453, 372 (2008).

[2.27] M. Saba, C. Ciuti, J. Bloch, V. Thierry-Mieg, R. André, Le Si Dang, S. Kundermann, A. Mura, G. Bongiovanni, J. L. Staehli and B. Deveaud : Nature 454 731 (2001).

Chapter 3

Characteristics of the two dielectric DBR GaN-VCSELs

3.1 Structure design

3.1.1 GaN-based VCSELs with two mirrors

In this study we propose a VCSEL structure consisting two dielectric DBRs and a GaN-based resonant cavity. An epitaxially grown, thick (~4 μm) GaN-based cavity incorporated with InGaN MQWs was separated from the sapphire substrate by using laser lift-off and then embedded the cavity between two dielectric DBRs. By using different dielectric materials with large difference in refractive index (for example, the difference in SiO_2 and TiO_2 is ~1.58 at 430 nm), a DBR with a high reflectivity and wide stop band could be achieved with less DBR pairs.

SiO_2/TiO_2 and SiO_2/Ta_2O_5 DBRs were used in our GaN-based VCSELs. The difference of refractive index between SiO_2 and TiO_2 is larger than that between SiO_2 and Ta_2O_5, therefore SiO_2/TiO_2 DBR can achieve a high reflectivity with less pair than SiO_2/Ta_2O_5 DBR. Since the absorption coefficient of Ta_2O_5 for the pumping laser (Nd:YVO_4 laser with laser wavelength of 355 nm) is smaller than SiO_2, SiO_2/Ta_2O_5 DBR was used in order to reduce the absorption of pumping laser as the pumping laser passes through the DBR. The thickness of p-GaN is chose to be 1.5λ in order to maximize the overlap between anti-node and MQWs. The structure for simulation is based on the fabricated dielectric DBRs VCSLEs. Figure 3.1 shows the simulated standing wave (square of electric field) patterns calculated by transfer matrix inside the cavity of the VCSEL structure [3.1]. The numerical simulated indicates that the ten pairs MQWs cover whole half λ optical field, therefore the resonant modes in the cavity can be amplified efficiently. The thick n-type GaN layer in the structure can prevent the damage on the InGaN/GaN MQWs since the dislocation or defect might migrate into the MQWs during the laser lift-off process [3.2]. From the numerical simulation of the VCSEL structures with different p- and n-GaN thickness, we also found that the overlap between optical field and MQWs strongly depends on the thickness of p-GaN layer, but not on the thickness of the n-type GaN. In addition, since the MQW region with 1/2λ optical thickness can compensate the possible misalignment between the anti-nodes of the standing wave pattern and the active region position, the effect of the thickness variation of n-GaN that can not be controlled preciously during laser lift-off can be minimized.

3.1.2 Laser lift-off technique

In 1999, Song *et al.* demonstrated a dielectric DBR VCSEL structure consisting of InGaN MQWs and 10-pair HfO_2/SiO_2 top and bottom DBR using laser left-off (LLO) technology [3.3]. The reflectivity of top and bottom DBRs were 99.5% and 99.9%, respectively. Now, we also use the same technique to fabricate our sample. Then, the bonding energy of GaN is high as 8.92 eV/molecule, results in the higher melting temperatures and good thermal stability of the GaN compounds compared to other compound semiconductors. The activation energy for GaN decomposition is 3.25 eV/atom. As to the observation of Ga droplets during decomposition in vacuum indicating that GaN decomposes into solid gallium and gaseous nitrogen was reported by Groh et al [3.4]. Sun et al. [3.5] found the thermal decomposition of MOCVD grown GaN on r-plane sapphire occur at a temperature of 1000 ^{o}C in a hydrogen ambient. Their report indicated decomposition of the $GaN \rightarrow 2Ga(l)+N_2(g)$ will occur at a critical temperature of ~1000 ^{o}C at atmospheric pressure [3.4, 3.6]. In this study, a KrF excimer laser with a wavelength of 248 nm (5 eV) was used to decompose the GaN grown on c-plane sapphire. The laser illuminated on the surface between GaN and sapphire and decomposed the GaN into Ga and N_2, hence, the grown GaN-based LED or micro-cavity structure were transferred from the sapphire substrate to host substrate.

3.1.3 Sample structure

The GaN/InGaN microcavity devices was fabricated by a standard epitaxial growth, followed by dielectric coating, laser lift off, and another dielectric coating to finally form a surface emitting microcavity. The device was grown on a (0001)-oriented sapphire substrate by metalorganic chemical vapor deposition (MOCVD). The layer structures are: a 30nm nucleation layer, a 4 μm GaN bulk layer, MQWs consisting of 10 periods of 5 nm GaN barriers and 3 nm $In_{0.1}Ga_{0.9}N$ wells, and a 200 nm GaN cap layer. The photoluminescence (PL) emission peak of the fabricated MQW was at 420 nm. Then, a 6 pairs of SiO_2/TiO_2 dielectric DBR was deposited on the top surface. In order to measure the spectral reflectivity of the deposited DBR, a glass substrate served as a monitor sample was deposited in the same deposition run. The reflectance spectrum of the SiO_2/TiO_2 DBR is obtained by measuring the monitor sample and the PL spectrum of the as-grown sample as shown by Figure 3.2. Next, a silica substrate was expoxied onto the BDR surface, which is nearly transparent to the wavelengths of the pumping laser and our VCSEL. In order to enhance the adhesion between the epitaxial layers and the silica substrate, an array of disk-like patterns with a diameter of 60 μm was formed by standard photolithography and the SiO_2/TiO_2 DBR mesas were formed using a buffer oxide etcher. A pulsed excimer laser was then focused through sapphire substrate onto sapphire GaN interface to remove sapphire substrate by thermal ablation. After the LLO process, the sample was dipped in HCl solution to remove residual Ga droplets on the exposed GaN buffer layers. In the next step, the sample was lapped and polished using diamond powders to smooth the GaN surface since the LLO process left a roughened surface. However, to prevent the possible degradation of the quality of MQWs during lapping, the 4.2 μm GaN bulk layer was preserved, followed by a eight pairs of SiO_2/ Ta_2O_5 DBR dielectric coating on the polished GaN surface. The final finished Fabry-Perot cavity formed by these two DBR mirrors has a vavity length of 4 μm. Figure 3.3 shows the complete sample structure and Figure 3.4 shows the fabrication process of the GaN-based dielectric DBRs VCSEL. Figure 3.5 (a) shows the microscopic image of a fabricated 2x2 VCSEL array and the circular areas are the locations of VCSELs with DBRs, also serving the emission apertures. Figure 3.5 (b) 、 (c) shows a photograph of the fabricated VCSEL on a silica host substrate and a Si substrate, respectively. In this chapter, we observed the characteristics of VCSEL bonded on the Si substrate.

3.2 Measurement setup

The fabricated two dielectric GaN-based VCSELs were optically pumped by a Nd: yttrium aluminum garnet (YAG) laser (PowerChip NanoLaser CDRH model, JDS Uniphase) whose lasing wavelength is 355 nm with a repetition rate of 1 k Hz and a pulse width of 0.5 ns, and the other source is 325 nm HeCd continuous wavelength (CW) laser. The system have two optical pumping sources, two optical incident paths, two methods for collecting photoluminescence and two ways to collect surface images of the sample as shown in Figure 3.6, then the setup mentioned before represents the so-called angle-resolved μ-PL (AR μ-PL) system. As shown in Figure 3.6, the incidence path of Nd: YVO_4 pulse laser whose laser beam was focused with a spot of x-axis about 50 μm and y-axis about 130 μm in an elliptical shape by a convex lens with 10 cm focus. It is obliquely incident on the VCSEL sample from the SiO_2/ Ta_2O_5 DBR in order to reduce the absorption of the pumping laser by the DBR. The light emission from the VCSEL sample was collected by a 15X objective lens and then straightly transmitted to a spectrometer (Jobin-Yvon IHR320 Spectrometer) with a spectral resolution of 0.07 nm or collected by a fiber with a 600 μm core. Also, the incidence path of HeCd CW laser whose laser beam was focused with a spot size of about 1 μm in diameter by an objective lens (x15) and is vertically incident on the VCSEL sample from the SiO_2/ Ta_2O_5 DBR. The light emission from the sample was gathered by a 15X objective lens and straightly collected by spectrometer, too. The samples are optically pumped by laser beam with an incident angle of 0° or 60° for measuring the divergent angle. The VCSEL sample was put in a cryostat chamber for measuring the temperature dependent characteristics. In addition, a charge-coupled device (CCD) camera was used to locate the aperture and observe the emission patterns of the VCSEL.

3.3 Threshold condition and spectrum evolution

Figure 3.7 indicates that pumping energy is below the threshold, meanwhile, the spontaneous emission spectrum have multiple cavity modes. The cavity length of the VCSEL can be estimated by

$$\Delta\lambda = \frac{\lambda^2}{2(n - \frac{dn}{d\lambda}\lambda)L}, \qquad (3.1)$$

where λ is the wavelength of cavity mode, L is cavity length and $n - \frac{dn}{d\lambda}\lambda$ is refractive index of the cavity with taking wavelength dispersion into consideration. The cavity modes spacing show by the PL emission is about 7 nm corresponding to a cavity length of 4.2 μm, which is nearly equal to the thickness of the epitaxial cavity. The linewidth of each individual cavity mode is 0.4 nm. The cavity quality factor (Q factor), which is a measure of the shapness or selectivity of a resonant cavity, therefore cab be estimated from the ratio of wavelength to linewidth ($\lambda/\Delta\lambda$) is about 1000. Considering the optical absorption of the GaN layer, the estimated effective cavity reflectivity based on this Q factor is about 98%, which is close to the cavity reflectivity achieved by the two dielectric DBRs. This result indicates that the laser cavity structure was nearly intact after laser lift-off process. Figure 3.8 shows the evolution of the VCSEL emission spectrum under different pumping levels at room temperature. As the pumping energy increased, a lasing mode was obtained from one of the cavity modes that can be observed below threshold condition. Figure 3.9 shows laser emission intensity obtained from the emission spectra as a function of pumping energy at room temperature. As pumping energy increased above the threshold, a dominant laser emission line appeared at 412 nm with a narrow linewidth of about 0.26 nm. The lasing wavelength is located at one of the cavity modes near the peak emission wavelength of the InGaN MQWs. The pumping laser beam was focused with a spot size of about 80 μm, while the measurement setup will be introduced in Chapter 4. The threshold condition was obtained at a pumping energy of E_{th}=784 nJ corresponding to an energy density of 15.6 mJ/cm^2 and the inset represents one of the lasing conditions, whose pumping power is 0.89mW. Output laser intensity from the sample increased linearly with pumping energy beyond the threshold. The estimated carrier density at the threshold is on the order of 10^{20} cm^{-3} assuming that the pumping light with an emission wavelength of 355 nm has experienced a 60%

transmission through the SiO_2/Ta_2O_5 DBR layers and undergone a 98% absorption in the thick GaN layer. Figure 3.10 shows the far-field pattern (FFP) of the laser emission. The laser emission has a full-width at half maximum

(FWHM) of the FFP is about 5° in both horizontal and vertical directions. We measured the laser emission polarization contrast between two orthogonal directions by placing a polarizer in front of the entrance of the spectrum analyzer. The laser emission intensity varied as a function of polarizer rotation angle as shown in Figure 3.11. We used the curve with a function of sinθ to fit the angle dependent laser intensity. The difference between the two angles of minimum intensities is 180^{o} indicating the emission laser a linear polarization. The degree of polarization of the VCSEL emission is about 79.4% according to the definition of $P = \frac{I_{\max} - I_{\min}}{I_{\max} + I_{\min}}$, where I_{max} and I_{min} is the intensity maximum and minimum of the laser emission, respectively.

3.4 Temperature characteristic

The temperature dependence of the lasing threshold of the VCSEL is shown in Figure 3.12. The threshold pumping energy increased gradually with increasing temperature. From the activation dependence of E_{th} and the dependence of the threshold condition on the temperature can be expressed as $E_{th}(T) = E_0 \exp(T/T_0)$, where E_0 is a constant and T_0 is the characteristic temperature. We obtained a characteristic temperature of about 130 K for this dielectric type VCSEL for the temperature range of 70 to 300 K by linearly fitting the experimental result. This T_0 value is higher than the reported T_0 of 82 K or 120 k [3.7] for the GaN-based edge-emitting laser diode. High T_0 value could be attributed to a better gain-alignment of the MQWs with the cavity mode and a lower threshold carrier density due to the higher quality factor provided by both dielectric DBRs.

3.5 The gain characteristics for different temperature

3.5.1 Temperature dependent gain characteristics by a Nd: yttrium aluminum garent (YAG) laser

Figure 3.13 shows the photoluminescence spectra of the GaN-based VCSEL under different pumping power levels at 80 K. Above the threshold condition, only one lasing mode at about 407 nm dominates. The Hakki-Paoli method is one of the most common method to extract net optical gain from amplified spontaneous emission (ASE) spectra. Therefore, the optical gain can be therefore estimated using the Hakki-Paoli [5.14 pig] method to analyze these multiple cavity modes from the photoluminescence spectra below the threshold condition. To derive the net optical gain, we first consider a semiconductor laser in a Fabry-Perot cavity. The reflectivities of the two mirrors are R_1 and R_2, respectively. Now, a field P_1 incident on mirror 1 and the amplitude of the reflected wave is $R_1^{1/2}F_1$. This first reflection travels towards morror 2 with a propagation constant k-j (α_i/2), where α_i is the internal loss per unit length. When a wave bounces back and forth in a Fabry-Perot cavity, its amplitude after one round trip of distance 2L has to remain at least the same to obtain gain. When the multiple reflections interfere constructively and destructive, the total incident field in a single mode are

$$\begin{cases} P_1^+ = \dfrac{P_1}{1-(R_1R_2)^{1/2}e^{-\alpha_i L}}, constructive \quad \text{int}\,erference \\ P_1^- = \dfrac{P_1}{1+(R_1R_2)^{1/2}e^{-\alpha_i L}}, destructive \quad \text{int}\,erference \end{cases} \tag{3.1}$$

The maximum and minimum intensities with spectral measurements of Fabry-Perot modes in the cavity are I^+ and I, respectively. Therefore, α_i can be obtained from Eq. (3.1) and the structure is a VCSEL, which can be expressed as

$$G(\lambda) = -\frac{1}{\Gamma L}\ln\left[\frac{\left(I^{+}\right)^{\frac{1}{2}}+\left(I^{-}\right)^{\frac{1}{2}}}{\left(I^{+}\right)^{\frac{1}{2}}-\left(I^{-}\right)^{\frac{1}{2}}}\right]-\left(\frac{1}{2\Gamma L}\right)\ln\left(R_1R_2\right)+\frac{\alpha_i}{\Gamma} \tag{3.2}$$

whereλ is the wavelength at which the cavity modes are being measured. Confinement factor of the laser structure is estimated as $\Gamma = 0.7\%$ by calculating the spatial overlap between the optical field and MQWs layers in the VCSEL cavity, d_a is the thickness of ten quantum wells, I^+ and I^- are the maximum and minimum PL intensities for each cavity mode obtained from the measured PL spectra, R_1 and R_2 are DBRs reflectivities which are 99% and 98%, respectively, α_i is the average internal loss of the cavity, which is dominated by the absorption of thick GaN layer and was set to be 42 cm^{-1} at room temperature [3.8] and L is the cavity length. Under different pumping levels, the I^+ and I^- would vary and the individual gain for each cavity modes can be obtained from the eq. (3.2). The gain spectra of the VCSEL under different pumping power levels at 80 K are shown in Figure 3.14. Each data point was calculated from the corresponding cavity mode in Figure 3.13. The gain curves show an increasing trend as the pumping intensity increases and the gain bandwidth keeps broadening. In addition, the mode peaks blue shift due to the increase of the optical gain. At 80k, the peak gain of 2.2×10^{3} cm-1 was obtained at threshold condition with a carrier density of 6.8×10^{19} cm-^{3}. The gain spectra under different temperature (at 150K, 220K and 300K) were also obtained with the same measurement and calculation method, respectively. The pumping carrier density dependence of the peak gain of the lasing mode (at about 407 nm) is plotted in Figure 3.15 for different measurement temperature. Here the carrier density in QWs was estimated from the power density of the pumping laser assuming that the pumping light with the emission wavelength of 355 nm has experienced a 60% transmission through the SiO_2/Ta_2O_5 DBR layers and undergone a 98% absorption in the thick GaN layer with a absorption coefficient of 10^4 cm^{-1} [3.9]. At 80k, the threshold carrier density was estimated to be about 6.8×10^{19} cm^{-3}. The figure shows that the carrier density required to reach a given gain increases with increasing temperature and we can observe the gain increase more rapidly as a function of the injected carrier density at lower temperature. It could be resulted from several reasons: (1) The ratio of radiative to nonradiative recombination is lower at high temperature than that at low temperature. (2) The carrier overflow becomes pronounced at higher temperatures resulting in less radiative recombination in the MQWs and consequently a lower gain [3.10]. (3) The main cause is the broadening of Fermi occupation probability function which spreads carriers over a larger energy range for a given overall carrier density. The result is a lower spectral concentration of inverted carriers, which leads to a broadening of the gain spectrum.

Semiconductor lasers exhibit a strong variation of refractive index and optical gain when injected carrier concentration changes. The parameter describing this dependency is called linewidth enhancement factor (α-factor) [3.11]. It is an important parameter of semiconductor lasers, such as laser linewidth and chirp. We can estimate the linewidth enhancement factor from the ASE spectra below the threshold condition [3.12]. The α-factor is the ratio of the change of the refractive index (n) with carrier density (N) respect to the change in optical gain with carrier density and can be expressed by

$$\alpha = \frac{2\pi}{L\Delta\lambda}\frac{d\lambda}{dg} \qquad (3.3)$$

where $\Delta\lambda$ is the cavity mode spacing, L is the cavity length, $d\lambda$ is the wavelength shift when the carrier density is varied by dN, and dg is the change in optical gain with carrier density (*N*). Hence, the α-factor can be obtained from the emission spectra under different pumping power levels below the threshold from Eq. (3.3). The estimated α-factors under different temperature are shown in Figure 3.16. At the lasing mode, the α-factors decrease as the ever-declining temperature. The α values increase as the increasing temperature owing to the increment of carrier density in the QWs. For the lasing mode, the α-factors varied from 4.3 to 0.6 as the temperature varied from 300K to 80K. In comparison to the InGaN/GaN edge emitting laser structure that the α value varies between 2.5 and 10 [3.13], the linewidth enhancement factor in the GaN-based VCSEL structure is smaller.

3.5.2 Temperature dependent gain characteristics by a CW laser

The wells of MQWs for our sample are $In_{0.1}Ga_{0.9}N$. We utilize the micro-PL intensity mapping of the VCSEL with a scanning optical microscopy to measure the inhomogeneous photoluminescence caused by spatial inhomogeneity of In composition, as shown in Figure 3.17 (a). It shows the intensity mapping of the entire aperture of the VCSEL. With a fine scan inside the square area in Figure 3.17(a), Figure 3.17(b) shows the non-uniform PL emission intensity across the aperture has patches of bright areas with about 2~4 μm in size. The bright areas are higher intensity than the dark areas. Figure 3.18 shows the PL spectra of bright (marked as A) and dark (marked as B) areas. Nevertheless, spatial inhomogeneity in cavity loss due to potential micrometer-scale imperfection of the DBRs could also cause different threshold gains in spatial distribution. On the other hand, the different micro-PL intensities across the VCSEL aperture imply a non-uniform material gain distribution existed in InGaN/GaN MQW layers.

Figure 3.19 shows the photoluminescence spectra of the GaN-based VCSEL by CW laser under different pumping power levels at 80K: (a) the bright areas (A), (b) the dark areas (B). Use Hakki-Paoli method to obtain the gain spectrum. Figure 3.20 shows the gain spectra of the VCSEL under different pumping power levels at 80 K: (a) the bright areas (A), (b) the dark areas (B). Each data point was calculated from the corresponding cavity mode in Figure 3.19. We can discover that the gain values of the highest PL intensity are larger than the relatively one of the lower intensity. We found that there exists sharp slopes of gain spectra ranging from 400 nm to 420 nm, while the slopes of the gain spectra ranging from 420 nm to 445 nm are smooth. The possible reason might be the large difference absorption at near band gap (400 nm ~ 420 nm). Nevertheless, the difference absorption from the band gap between 420 nm and 445 nm is small.. Here the carrier density in QWs was also estimated from the power density of the pumping laser. The figure also shows that the carrier density required to reach a given gain increases with increasing temperature and we can observe the gain increase more rapidly as a function of the injected carrier density at lower temperature, as shown in Figure 3.21. The reasons just like them were mentioned before. We can find that the gain value estimated by pulse laser is larger than the one by CW laser because of the larger carrier density in MQWs.

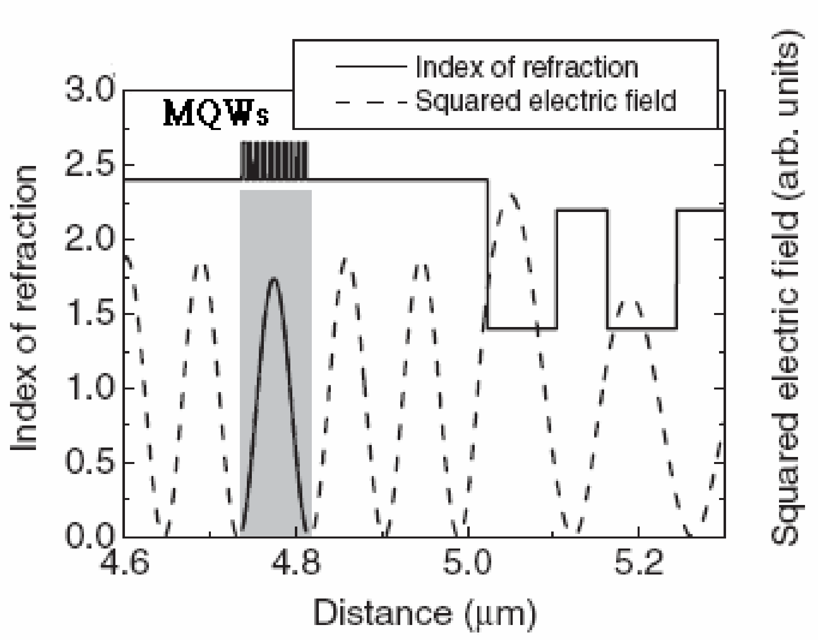

Figure 3.1 The simulated standing wave patterns inside the cavity for the dielectric DBRs VCSEL structure.

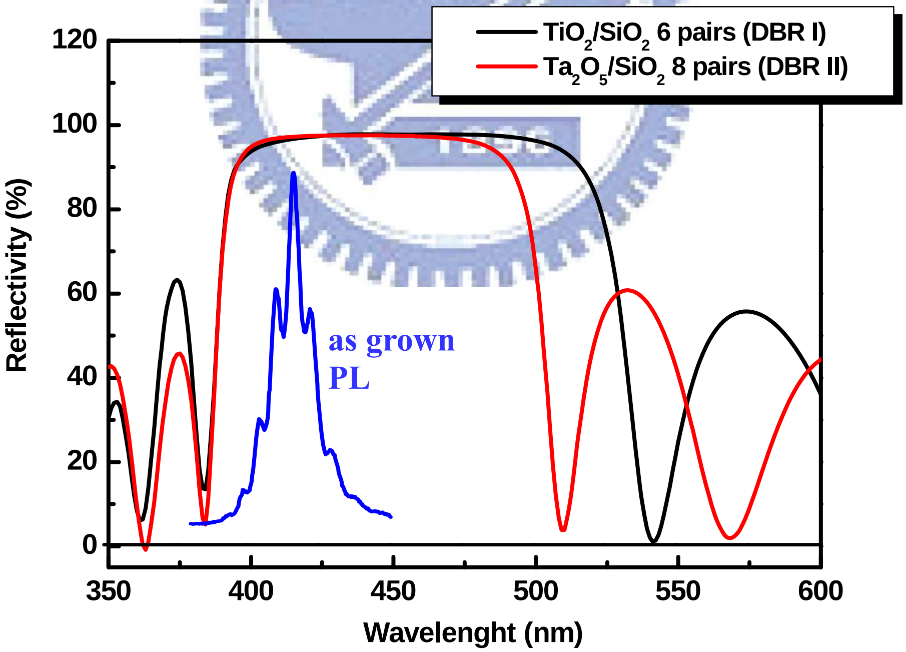

Figure 3.2 Measure spectral reflectivity of 6 pairs of SiO_2/TiO_2 DBR and 8 pairs of SiO_2/Ta_2O_5 DBR. The PL spectrum of the as grown cavity consists of 10 pairs of 5 nm GaN barriers and 3 nm $In_{0.1}Ga_{0.9}N$ wells.

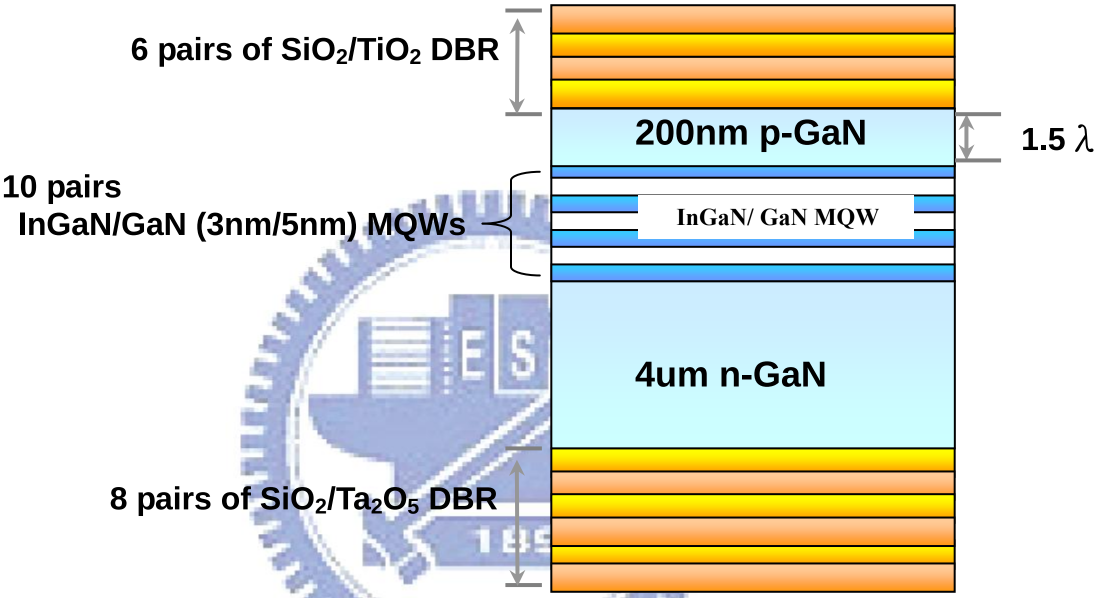

Figure 3.3 The layer structure used for calculation of standing wave patterns. The structure was constructed according to the fabricated dielectric DBRs VCSELs.

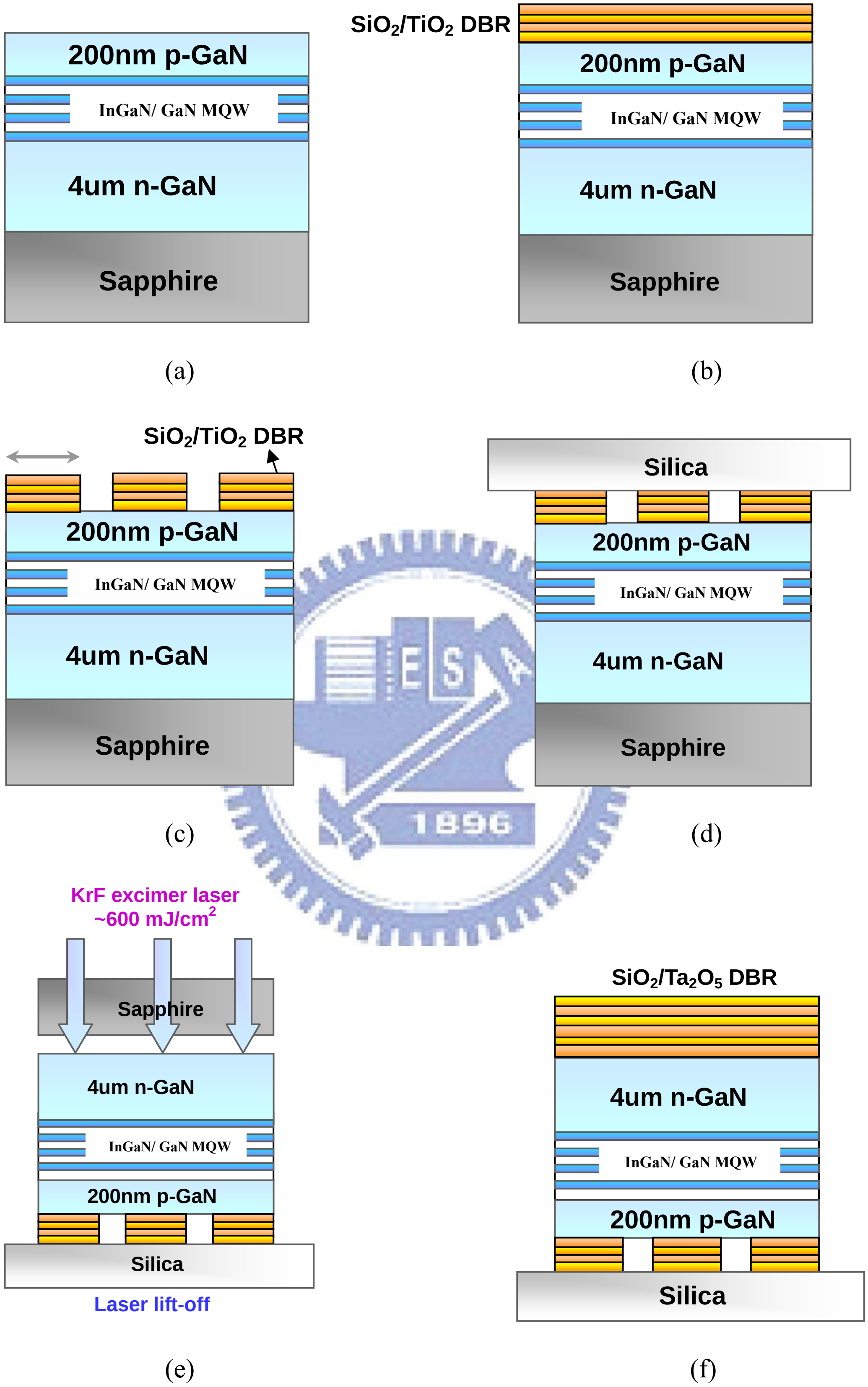

Figure 3.4 Fabrication of the GaN-based dielectric DBRs VCSEL.

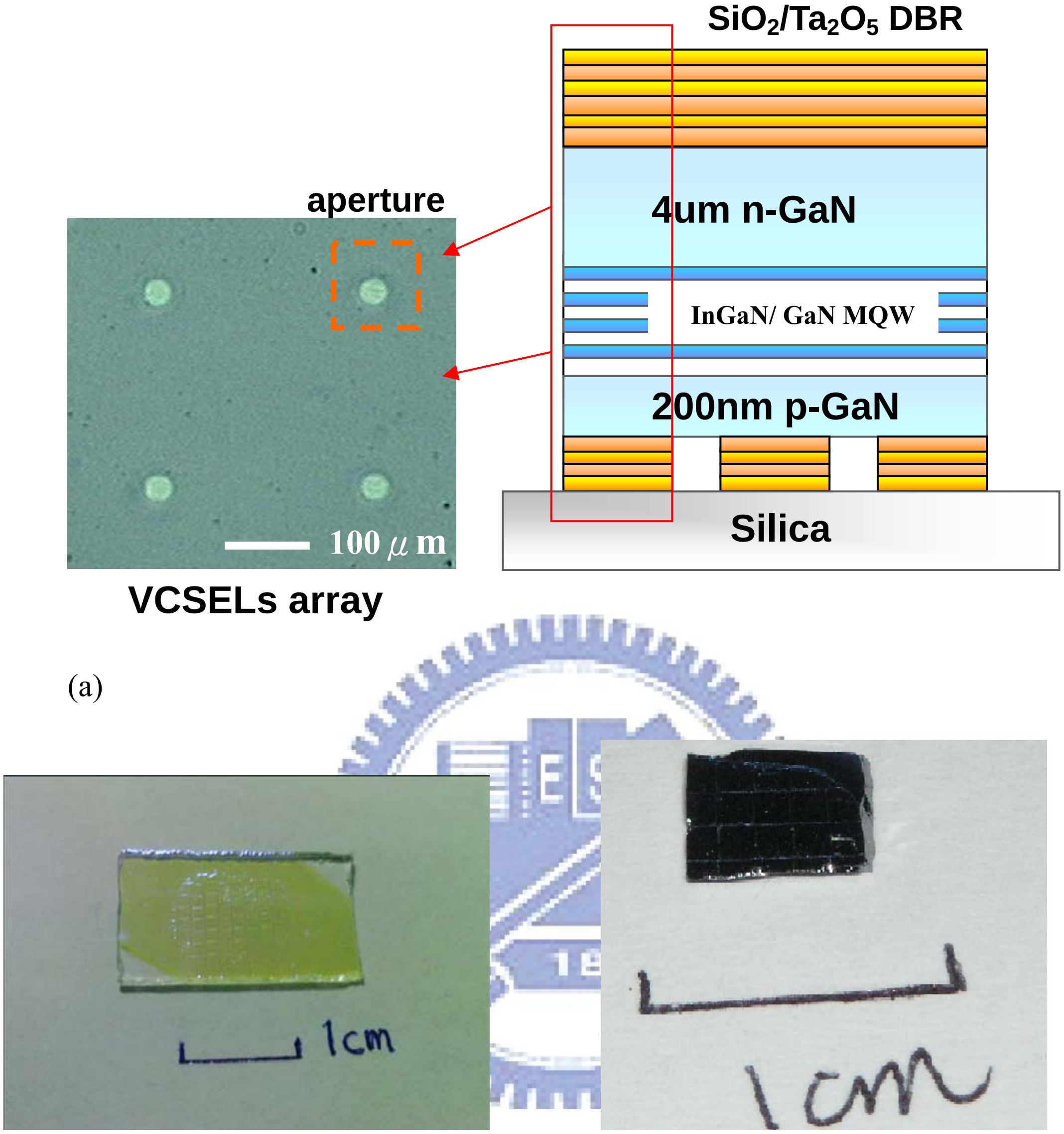

(a)

(b) (c)

Figure 3.5 (a) The left picture is the microscopic image of a fabricated 2x2 VCSEL array. The circular areas are the locations of VCSELs with DBRs, also serving the emission apertures. (b)、(c) A photograph of the fabricated VCSEL on a silica host substrate and a Si substrate, respectively.

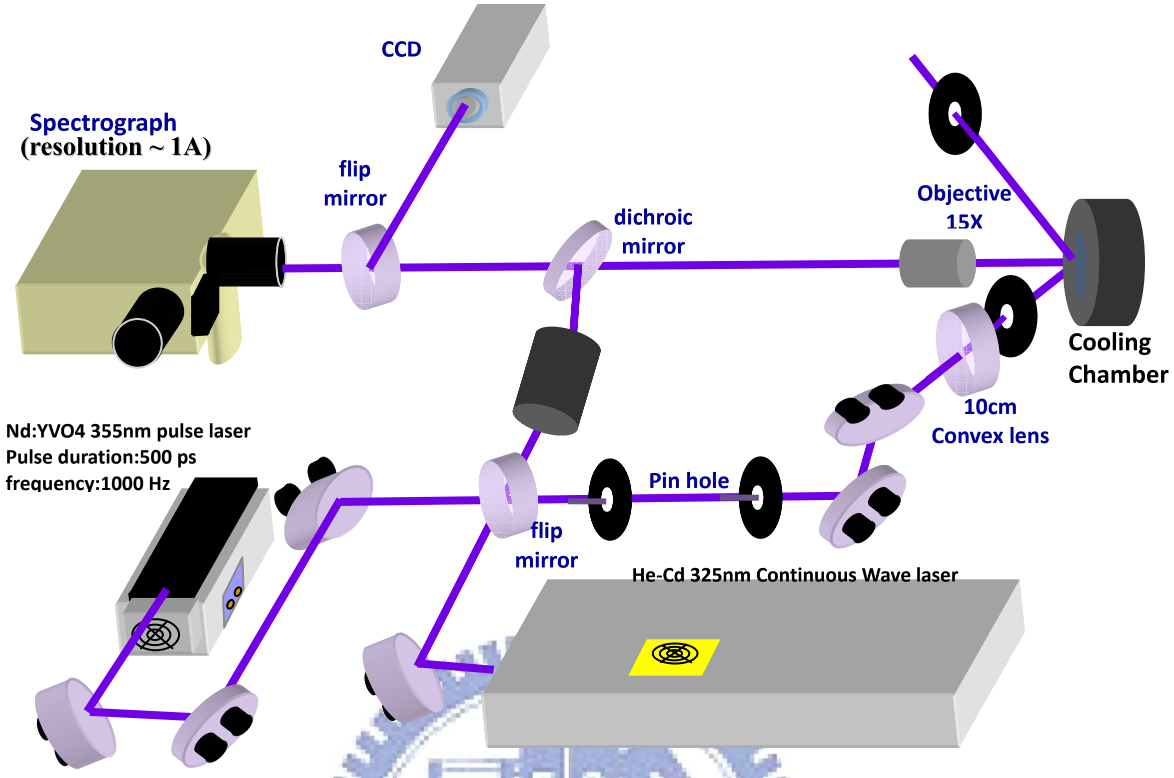

Figure 3.6 Schematic disgram of measurement setup for the characteristics of the GaN-based two dielectric DBRs VCSEL.

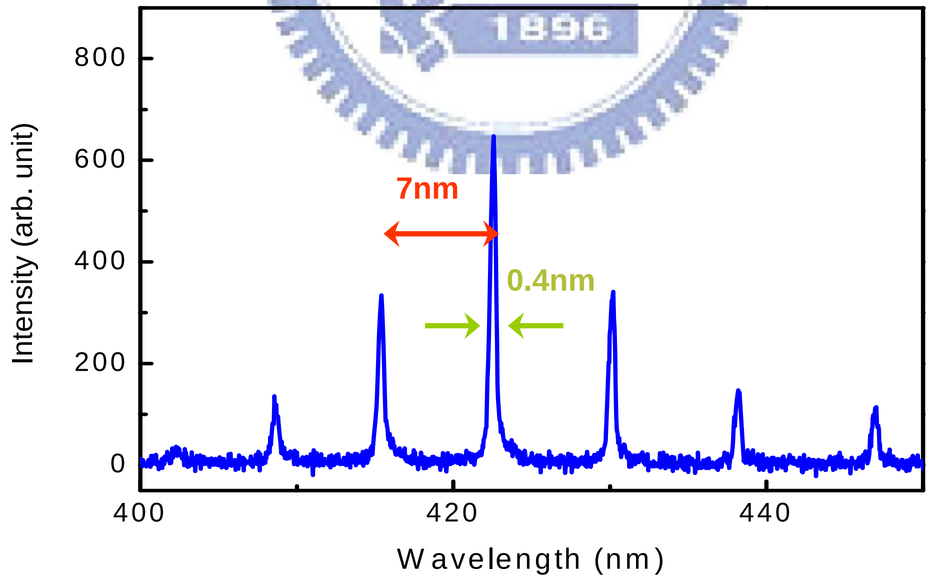

Figure 3.7 Spontaneous emission spectrum below threshold condition shows multiple cavity modes.

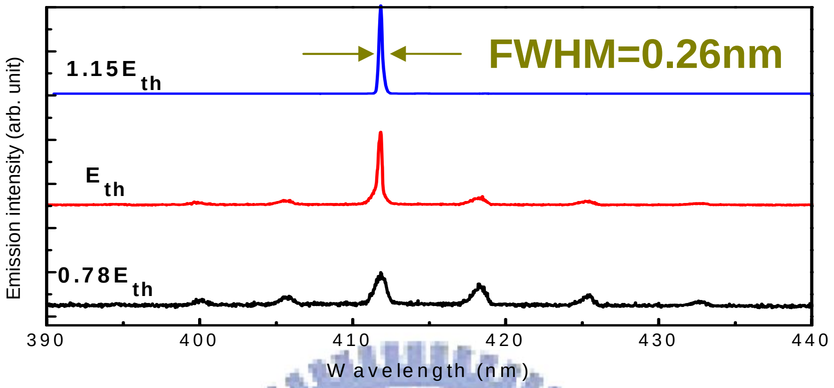

Figure 3.8 Spectral evolution of the VCSEL emission different pumping levels.

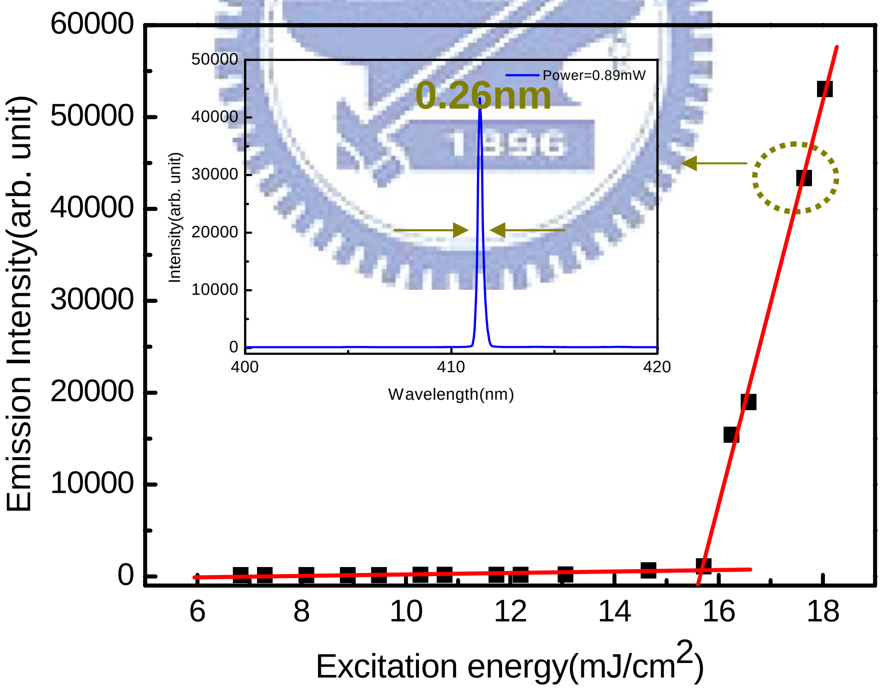

Figure 3.9 Laser emission intensity obtained from the emission spectra as a function of pumping energy at room temperature. The inset represents one of the lasing conditions, whose pumping power is 0.89mW.

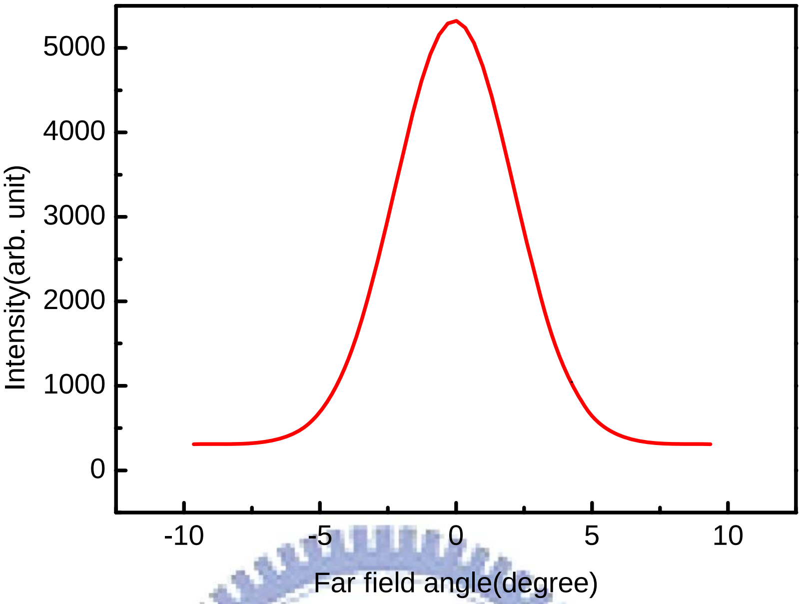

Figure 3.10 Far field pattern of the VCSEL.

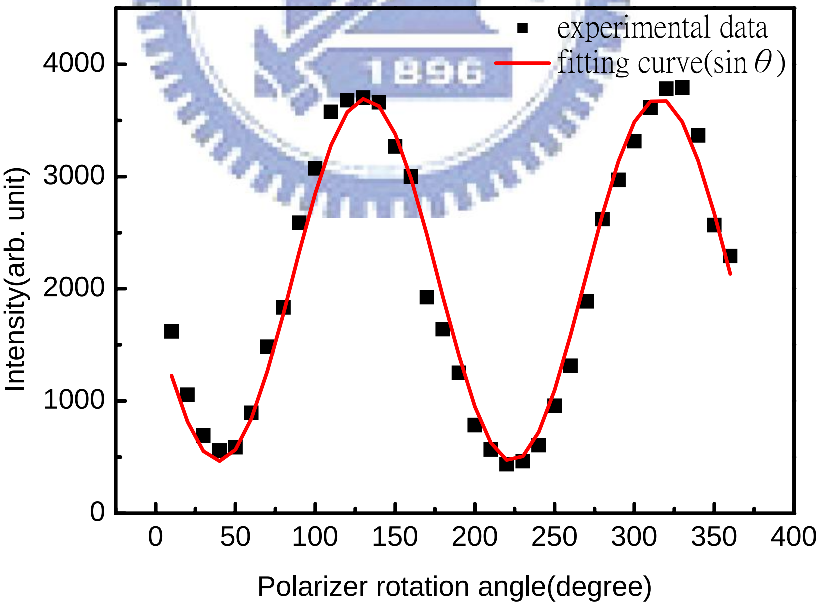

Figure 3.11 The angle dependent laser intensity

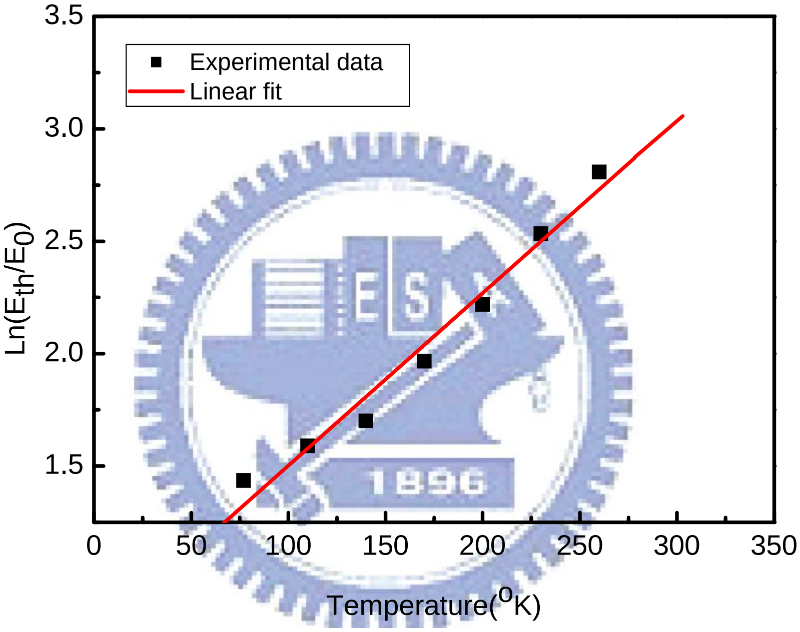

Figure 3.12 Temperature dependence of the lasing threshold of the VCSEL.

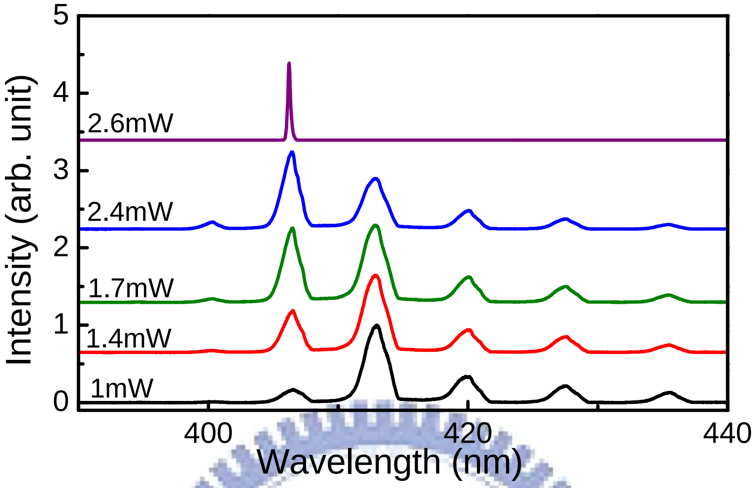

Figure 3.13 Photoluminescence spectra of the GaN-based VCSEL under different pumping power levels at 80 K.

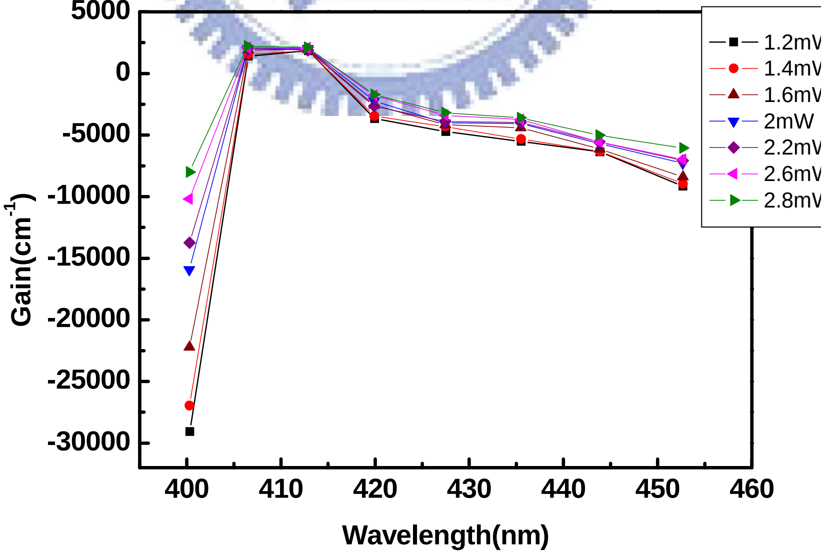

Figure 3.14 Gain spectra of the VCSEL under different pumping power levels at 80 K.

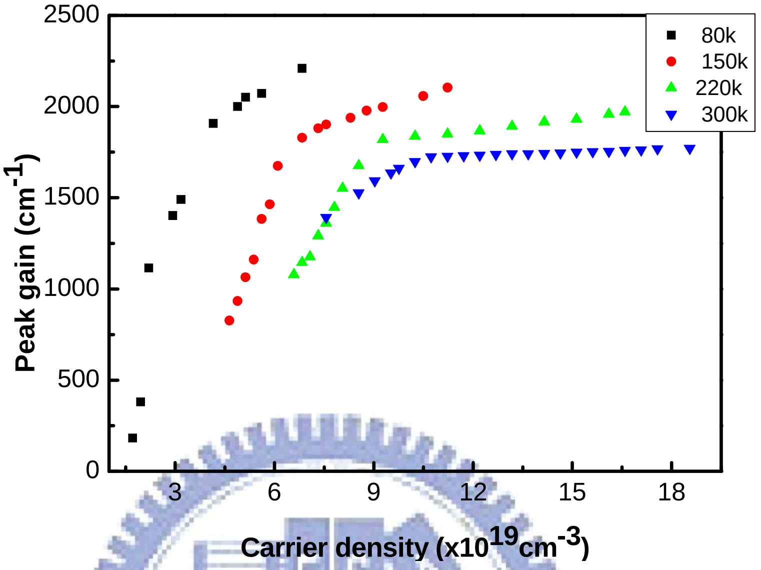

Figure 3.15 Pumping carrier density dependence of the peak gain of the lasing mode for different temperature

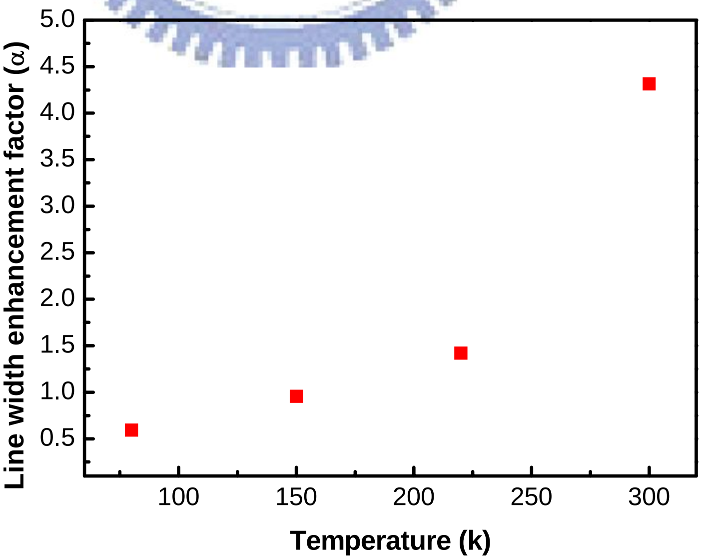

Figure 3.16 The α-factor value for different temperature

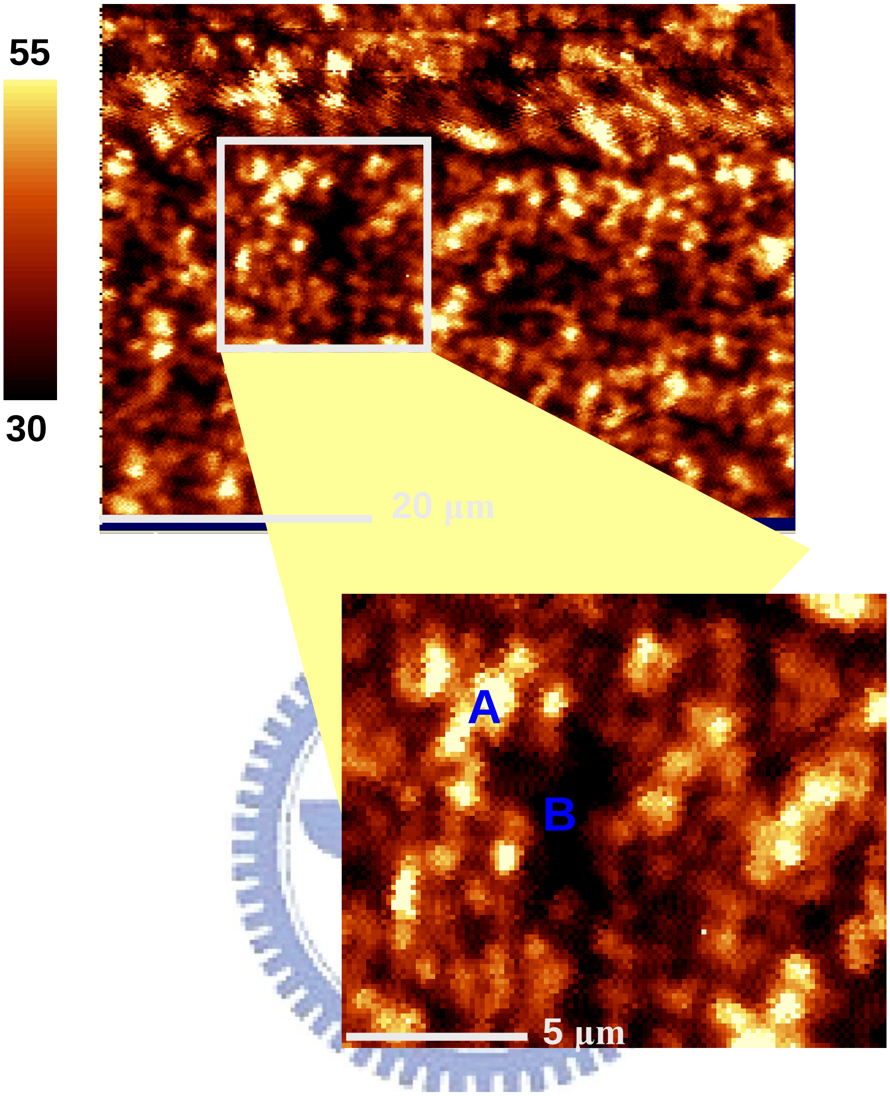

Figure 3.17 (a) Micro-PL intensity mapping image of the VCSEL aperture. (b) Fine micro-PL scan inside the square area in (a).

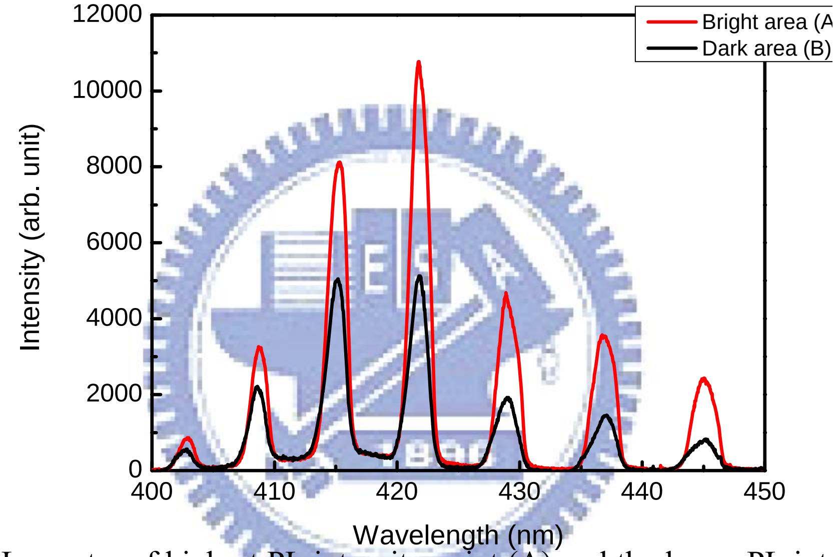

Figure 3.18 PL spectra of highest PL intensity point (A) and the lower PL intensity point (B).

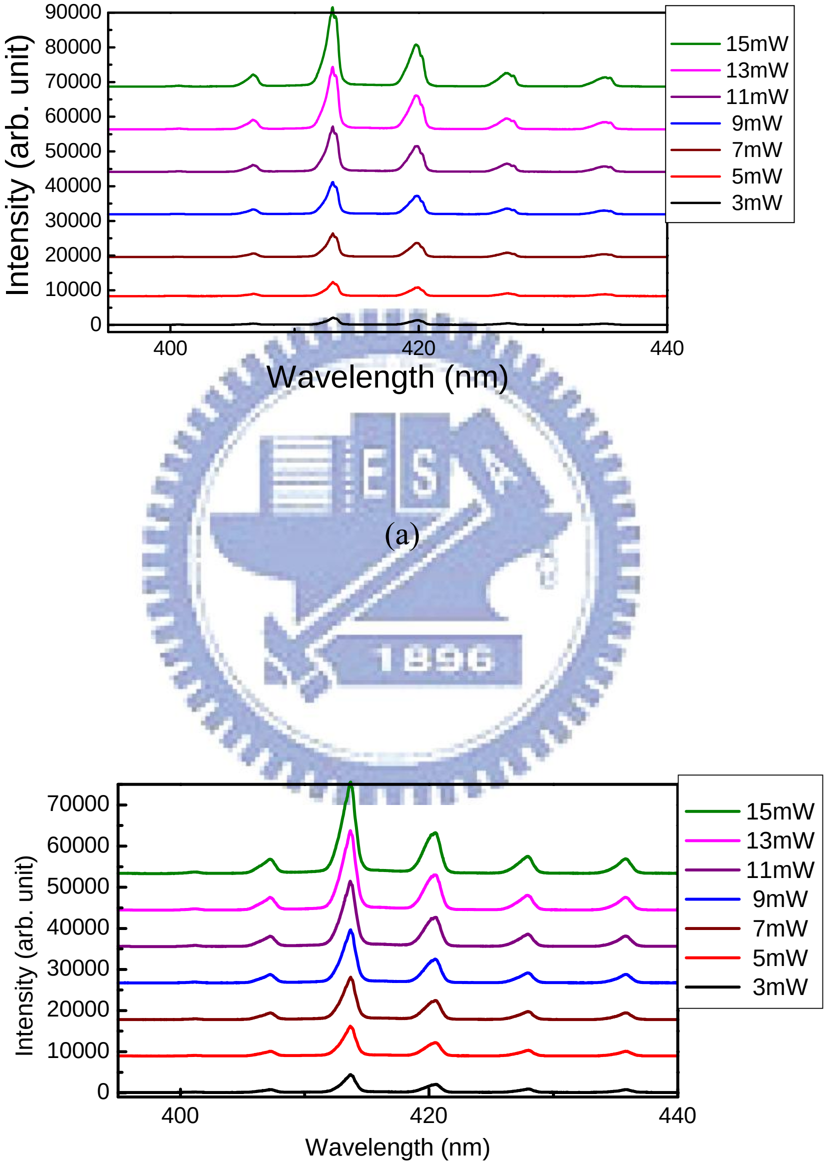

(a)

(b)

Figure 3.19 Photoluminescence spectra of the GaN-based VCSEL under different pumping power levels at 80k (a) the bright areas (A), (b) the dark areas (B).

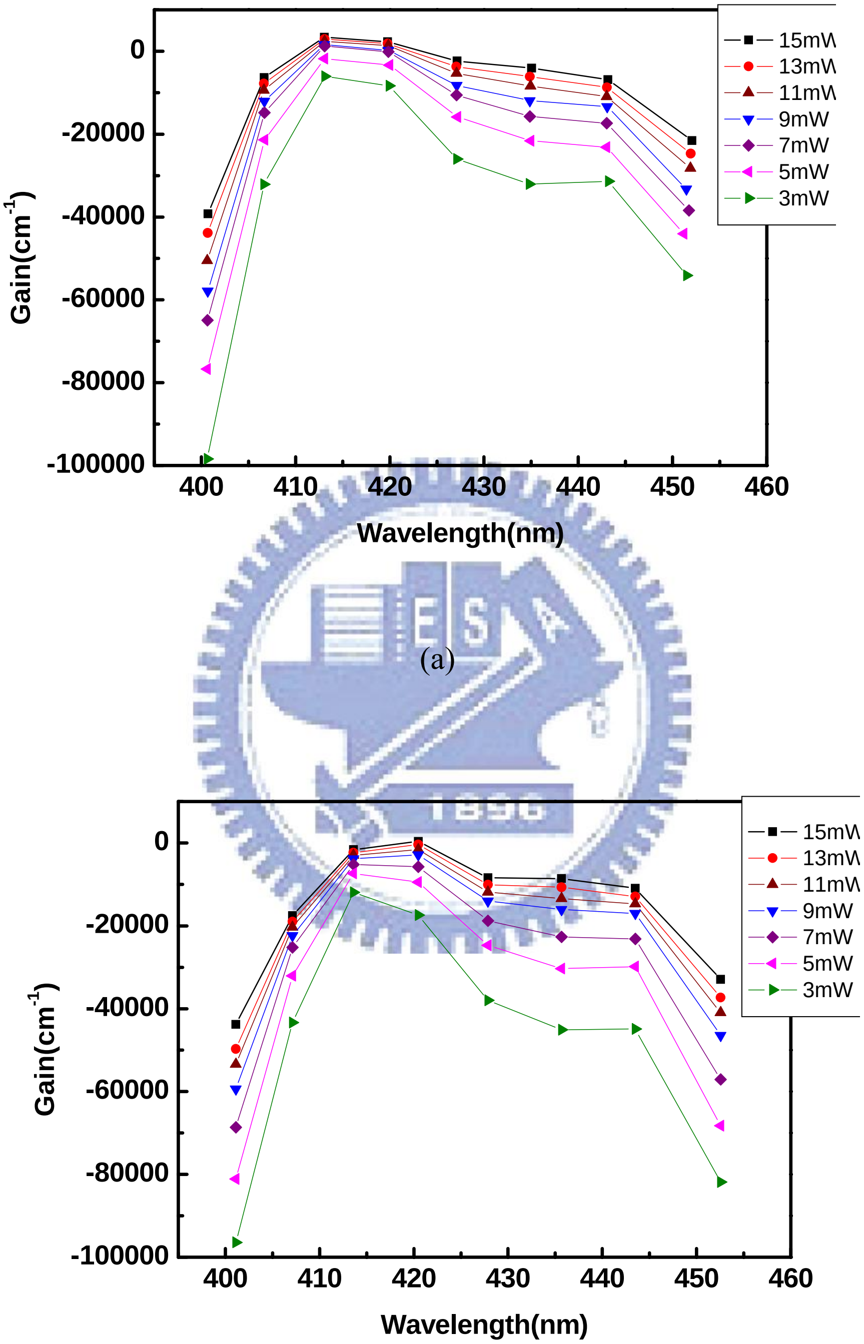

(a)

(b)

Figure 3.20 Gain spectra of the VCSEL under different pumping power levels at 80k.(a) the bright areas (A), (b) the dark areas (B).

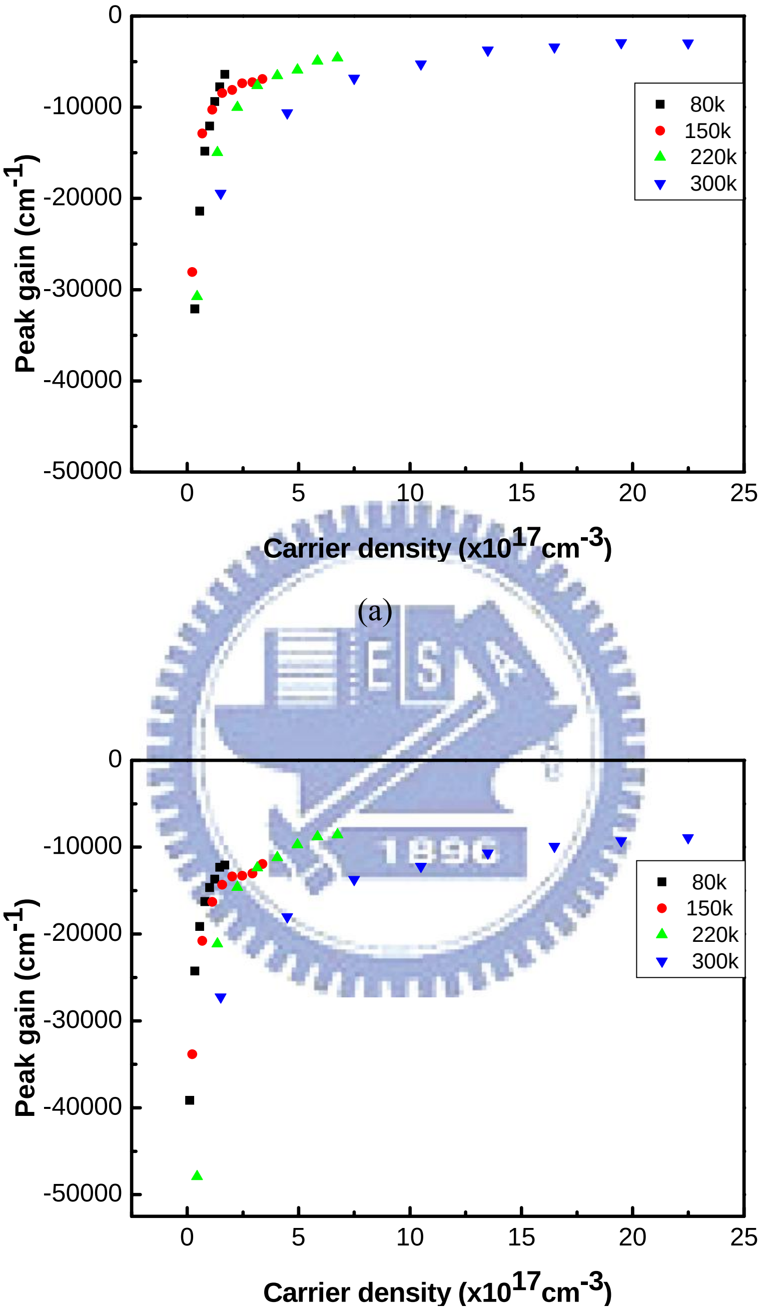

(a)

(b)

Figure 3.21 Pumping carrier density dependence of the peak gain of the lasing mode for different temperature (a) the bright areas (A), (b) the dark areas (B).

Reference

[3.1] J.T. CHU, T.C. Lu, H.H. Yao, C.C. Kao, W.D. Liang, J.Y. Tsai, H.C. Kuo, and S.C. Wang: Japanese Journal of Applied Physics 45, 2556 (2006).

[3.2] P. R. Tavernier and D. R. Clarke: J. Appl. Phys. **89**, 1527 (2001).

[3.3] Y.-K. Song, H. Zhou, M. Diagne, I. Ozden, A Vertikov, A. V. Nurmikko C. Carter-Coman, R. S. Kern, F. A. Kish, and M. R. Krames: Appl. Phys. Lett. **74**, 3441 (1999)

[3.4] R. Groh, G. Gerey, L. Bartha, and J.I. Pankove: Phys. Stat. Sol. A **26**, 353 (1974)

[3.5] C.J. Sun, P. Kung, A. Saxler, H. Ohsato, E. Bigan, and M. Razeghi: J. Appl. Phys. **76**, 236 (1994)

[3.6] M. E. Lin, B. N. Sverdlov, and H. Morkoç: Appl. Phys. Lett. **63**, 3625 (1993)

[3.7] C. Skierbiszewski, P. Perlin, I. Grzegory, Z. R. Wasilewski, M. Siekacz, A. Feduniewicz, P. Wisniewski, J. Borysiuk, P. Prystawko, G. Kamler, T. Suski, and S. Porowski: Semicond. Sci. Technol. **20**, 809 (2005)

[3.8] U. T. Schwarz, E. sturm, W. Wegscheider, V. Kummler, A. Lell, and V. Harle: Appl. Phys. Lett. **83**, 4095 (2003)

[3.9] M. O. Manasreh: Phys. Rev. B **53**, 16425 (1996)

[3.10] A. V. Sakharov, W. V. Lundin, I. L. Krestnikov, V. A. Semenov, A. S. Usikov, A. F. Tsatsul'nikov, Yu. G. Musikhin, M. V. Baidakova, and Zh. I. Alferov: Appl. Phys. Lett. **74**, 3921 (1999)

[3.11] C. H. Henry: IEEE J. Quantum Electron. **18**, 259 (1982)

[3.12] I. D. Henning and J. V. Collines: Electron Lett. **19**, 972 (1983)

[3.13] K.G. Gan and J. E. Bowers: IEEE Photon. Tech. Lett. **16**, 1256 (2004)

Chapter 4

Characteristics of semiconductor microcavity

4.1 Sample structure and measurement setup

The sample structure is as same as the above structure in chapter 3 except for the latter is bonded on silica, as shown in Figure 2.6 (b). Figure 4.1 shows the measurement setup. The fabricated microcavity was pumped by a CW HeCd laser through the SiO_2/Ta_2O_5 DBR mirror at room temperature. The laser was focused by a 15X objective with spot size about 1 μm. The PL emission was focus by the same objective and coupled into a fiber (100 μm in diameter) using an imaging optic and led to a spectrometer (Jobin-Yvon Triax 320) with a spectral resolution of 0.1 nm. In addition, a charge-coupled device (CCD) camera was used to locate the aperture and observe the emission patterns of the VCSEL.

4.2 Strong cavity polariton dispersion in multimode GaN microcavity

The PL spectra at different pump power levels are shown in Figure 4.2(a) along with a zoom in Figure 4.2 (b) around the GaN wavelength region. The GaN and InGaN QW transitions, 365 nm and 420 nm, were both excited. Multimode peaks can be identified from 370 nm all the way to 470 nm. Multiple Lorentzian profiles are used to fit the spectral peaks from 360 nm to 390 nm to identify their exact locations. Two typical fitting results are shown in Figure 4.2 (c) and (d) for high and low pump power levels. The sums of the fitted Lorentzian profiles are also displayed and both show fairly good fits. For those peaks can be clearly identified, the fitted peak position do not have noticeable changes within the range of different pump power levels. The mode spacing decreases by almost a factor of five from 470 nm to 370 nm. It could be attributed to one of the two reasons: (1) the material index dispersion, (2) the polariton dispersion. Because the top and bottom DBR are not a pair of perfect reflective mirrors, we must consider the induced phase shift in the cavity, as shown in Figure 4.3. We can find the variance of the phase for different wavelength as the blue curve depicted in Figure 4.3, while the red curve is the reflectivity of DBR.

Firstly, we discuss that if the material index dispersion cause the mode spacing to decrease gradually from 470 nm to 370 nm. A theoretical index dispersion equation derived from semiconductor near band edge absorption and Kramers-Krong relation [4.1,4.2]

.
$$n(\hbar\omega) = \sqrt{C(x) + A(\hbar\omega / E_g)^{-2}(2 - (1 + \hbar\omega / E_g)^{1/2} - (1 - \hbar\omega / E_g)^{1/2}} \qquad (4.1)$$

where $\hbar\omega$ is the photon energy. E_g is the direct band gap of $Al_xGa_{1-x}N$, C is photon energy independent for a fixed Al content, A(x) have a relationship with photon energy and oscillator strength of the optical transition. Our sample is GaN-based, so the Al content is zero [4.3]. The blue curve is the refractive index of a similar GaN sample without DBR cavity measured by an ellipsometer, then we use the red curve out of eq. (4.1) to fit the blue curve, which show a fairly good agreement to our fit, as shown in Figure 4.4. The measured index dispersion along with the effective index dispersion $n_{PL}(\lambda_m)$ derived from the resonant peaks of PL spectrum are shown with blue square legends in Figure 4.5. The effective index $n_{PL}(\lambda_m)$ is obtained by the resonant condition

$$L = \frac{(m + 1 - \frac{\phi}{\pi})\lambda_m}{2n_{PL}(\lambda_m)} \qquad (4.2)$$

where L is the cavity length, m is the mode number, and $\lambda_m s$ are the observed PL peaks. Since we know the cavity length is L = 4.2 μm, ϕ is the phase degree, and mode number start from m = 43 from the above curve fitting, we can obtain $n_{PL}(\lambda_m)$. C, A, and energy band gap E_g are fitting parameters. Figure 4.5 shows the fitting of index dispersion disagree with the $n_{PL}(\lambda_m)$ value.

Secondly, we discuss the effect of polariton dispersion. In the strong interaction regime, exciton and photon form two coupled cavity polariton states. The two polariton states, upper and lower branch, have an unique anti-crossing dispersion characteristic. The observed resonant frequencies versus cavity axial mode wave numbers are shown with red square legends in Figure 4.6. The observed peaks are fitted by the lower branch cavity polariton dispersion equation, $\omega_{pol,n} = (\Omega + \omega_n)/2 - \sqrt{(\Omega - \omega_n)^2 + 4g^2}/2$, where Ω is the exciton frequency, ω_n is the photon frequency of nth cavity mode, which is concerning about the DBR phase shift, and it could be expressed as $\omega_n = (m + 1 - \frac{\phi(\lambda)}{\pi})\frac{c}{2nL}$, $\omega_{pol,n}$ is the corresponding polariton frequency, and *g* is the exciton photon interaction constant. The blue line is the fitted curve and it shows an excellent fit with the fitting parameters, $\hbar\Omega$ = 3.50 eV, $\hbar g$ = 0.29 eV, and n = 2.4. The exciton energy $\hbar\Omega$ = 3.5 eV from fitting is reasonably close to the 3.45 eV value cited in literatures. The exciton and photon energies versus wave number *k* obtained from the curve fitting are shown with two straight lines where the black triangle legends are the cavity photon modes coupled to excitons to form cavity polaritons. The interaction constant of $\hbar g$ = 290 meV is the highest value reported so far to the best of our knowledge. It is an order of magnitude larger than the recently reported state of the art values obtained from Rabi splitting measurement in III-nitride based devices, where Rabi splittings $\Omega_{RS} = 2\hbar g$ of 50meV and 56meV were reported for $3\lambda/2$ and 3λ cavity respectively [4.4,4.5]. The PL resonant peaks on the other hand are well described by the polariton dispersion equation as shown in Figure 4.6. This confirms that the observed PL peak dispersion can not be solely attributed to material dispersion and the full consideration of the interaction between exciton and cavity photons is required to explain the observed PL spectrum. There are some subtleties in PL spectra worth of attention. First, the upper polariton modes were not observed. We remark that it is probably because the energy levels of upper polariton are many times of thermal energy higher and are thermalized by a Boltzmann distribution factor with respect to those of the lower polaritons [4.6].

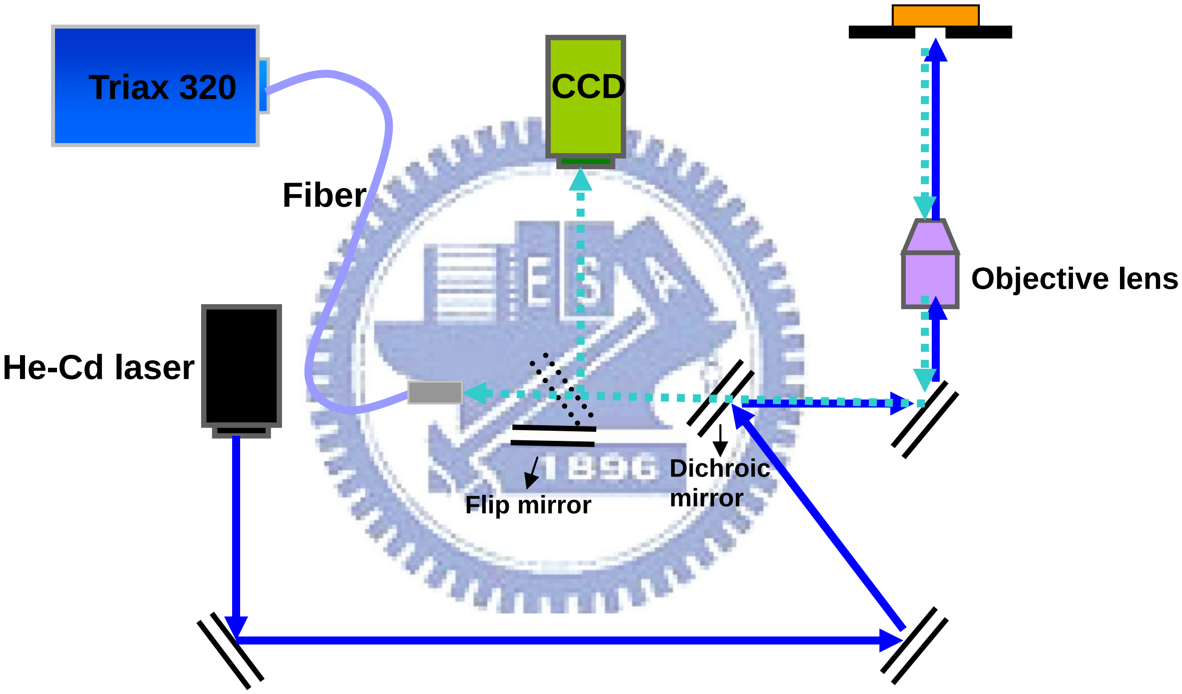

Figure 4.1 Schematic diagram of measurement setup.

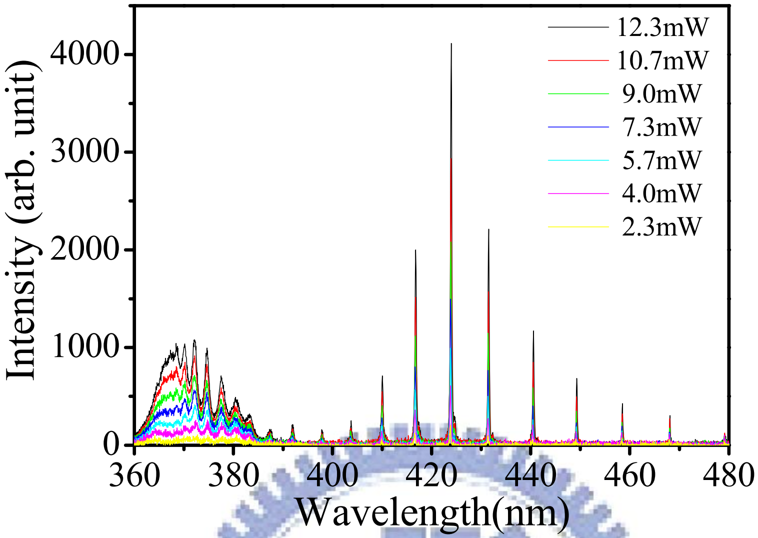
12.3mW
10.7mW
9.0mW
7.3mW
5.7mW
4.0mW
2.3mW
Intensity (arb. unit)
0
1000
2000
3000
4000
360
380
400
420
440
460
480
Wavelength(nm)

(a)

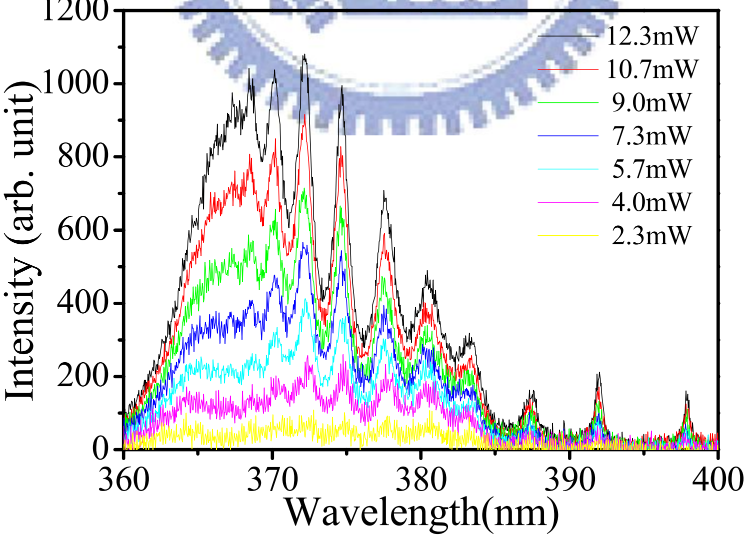
12.3mW
10.7mW
9.0mW
7.3mW
5.7mW
4.0mW
2.3mW
Intensity (arb. unit)
0
200
400
600
800
1000
1200
360
370
380
390
400
Wavelength(nm)

(b)

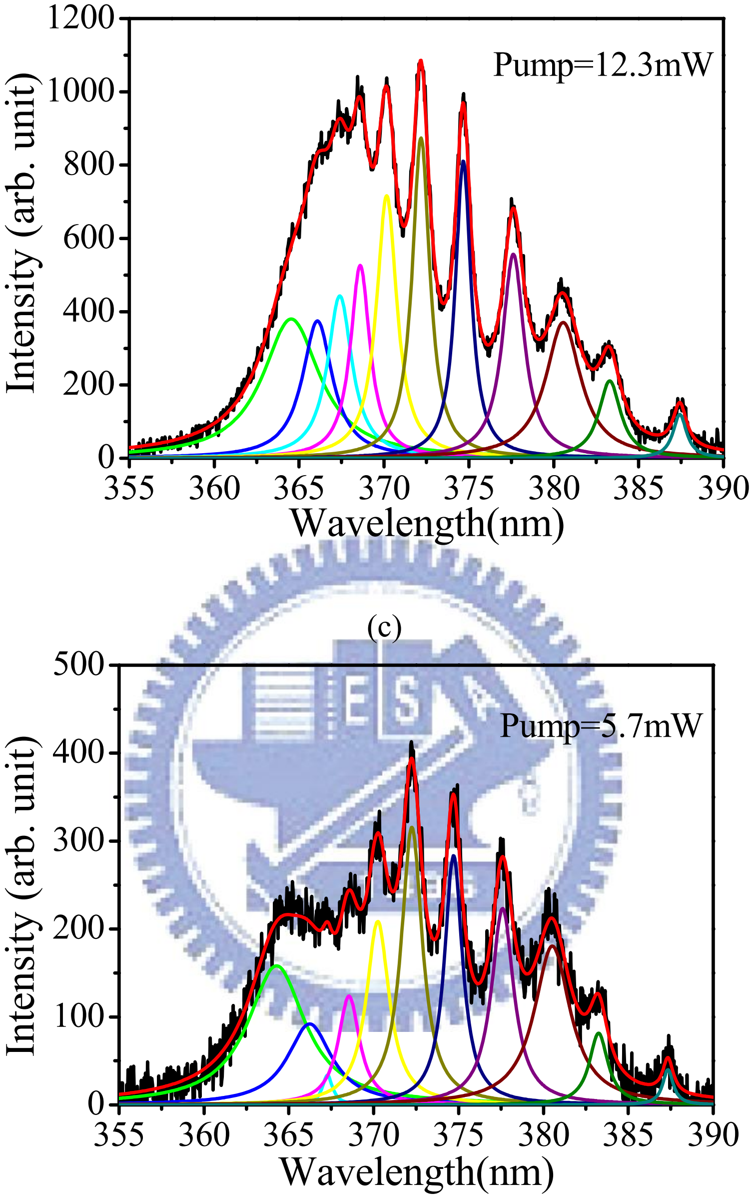

(c)

(d)

Figure 4.2 The PL spectra of optically pumped GaN/InGaN surface emitting microcavity. (a) PL spectra at various pump power levels. The GaN and InGaN/GaN QW transitions are both excited. The resonant spacing decreases by almost a factor of five from 470 nm to 370 nm. (b) A zoom in spectrum around GaN transition wavelength region. (c) (d) Typical multiple Lorentzian profile fitting along with the sums of the fitted profiles superimposed on PL spectra.

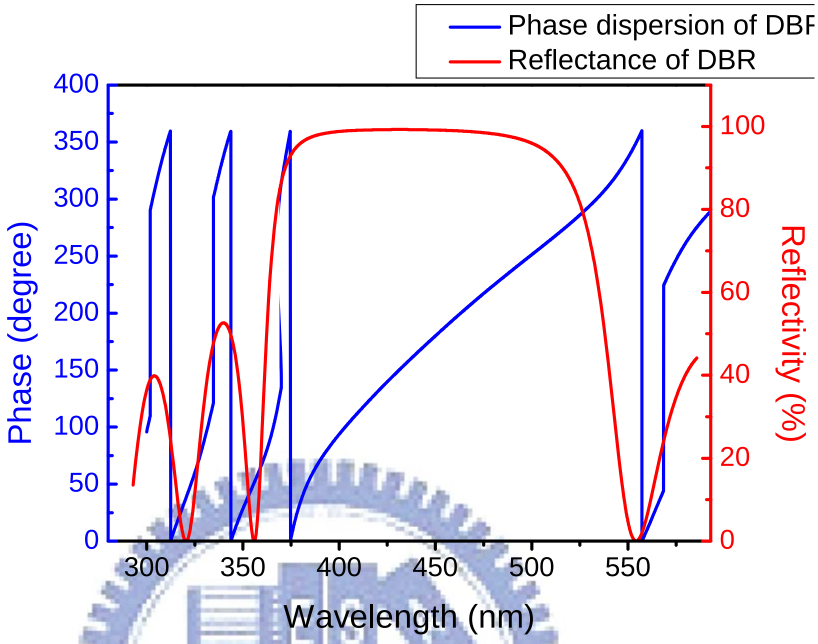

Figure 4.3 Phase shift and reflectance of DBR

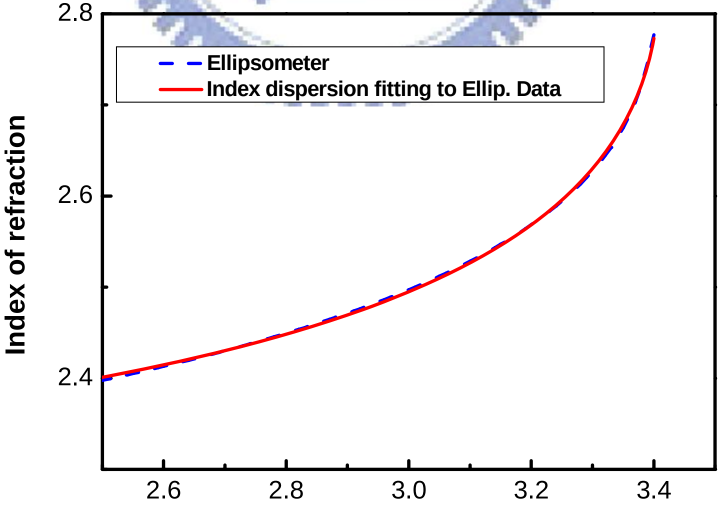

Figure 4.4 The index of refraction measured by ellipsometer (blue curve) is fitted by a theoretical index dispersion equation (red curve).

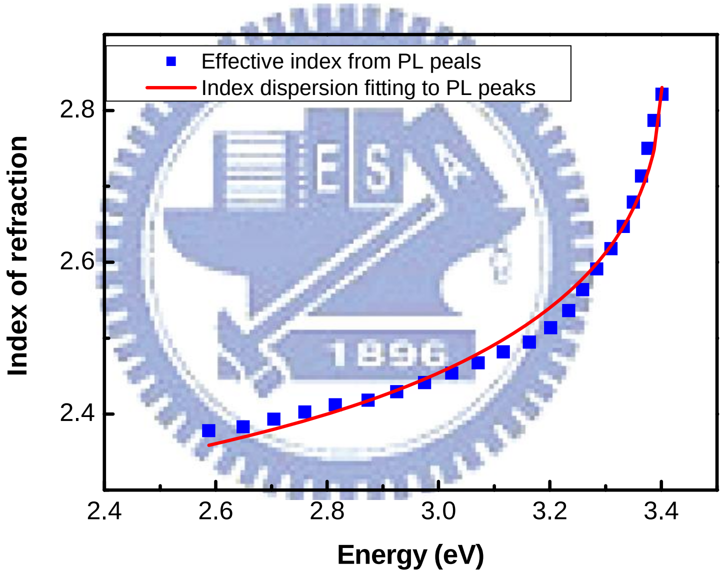

Figure 4.5 The effective index from PL resonant peaks (blue square legend) are fitted by a theoretical index dispersion equation (red curve).

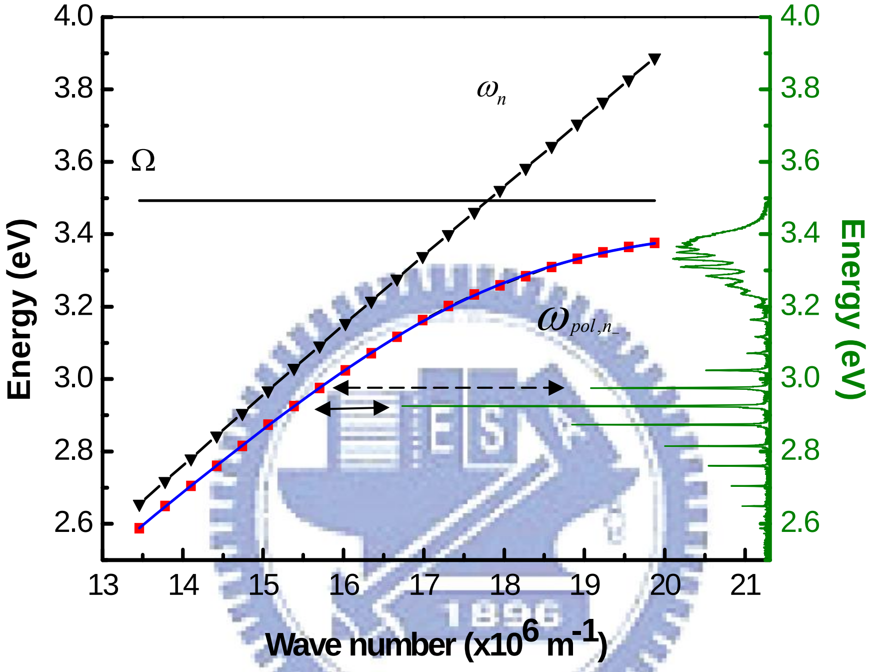

Figure 4.6 The red square legends are the observed multimode energy positions plotted versus equally spaced wave numbers. The blue line is the fitted curve based on cavity polariton dispersion equation. The two straight lines are the exciton and photon energies obtained from fitting parameters. The black triangle legends are the corresponding cavity photon modes.

Reference

[4.1] P.Y. Yu and M. Cardona: *Fundamentals of Semiconductors* (Springer, Berlin,1996)

[4.2] D. Brunner, H. Angerer, E. Bustarret, F. Freudenberg, R. Hopler, R.D. and O. Ambacher, and M. Stutzmann: Appi. Phys. Lett. 82,5090 (1997)

[4.3] D. Brunner, H. Angerer, E. Bustarret, F. Freudenberg, R. Ho¨ pler, R. Dimitrov, O. Ambacher,a) and M. Stutzmann: J. Appl. Phys. 82,5090 (1997)

[4.4] G. Christmann, R. Butte, E. Feltin, A. Mouti, P.A. Stadelmann, A. Castiglis, J.-F. Carlin, and N. Grandjean: Phys. Rev. B 77,085310 (2008).

[4.5] G. Christmann, R. Butte, E. Feltin, J.-F. Carlin, and N. Grandjean: Appl. Phys. Lett. 93 051102 (2008).

[4.6] R.P. Stanley, R. Houdre, C. Weisbuch, U. Oesterle, and M. Ilegems: Phys. Rev. B 53,10995 (1996)

Chapter 5

Conclusions and Future Work

5.1 Conclusion

5.1.1 Two dielectric DBRs VCSELs

We proposed a GaN-bsed VCSEL structure consists of InGaN/GaN MQWs and two dielectric DBRs with high reflectivity. The GaN-based cavity including MQWs was gown on a sapphire substrate. Then the grown cavity was embedded by two dielectric DBRs and transferred onto a silica substrate or a Si substrate.

The laser emission characteristics of a GaN-based vertical-cavity surface-emitting laser with two dielectric distributed Bragg reflectors were investigated under optically pumped operation at room temperature. The Q factor of the VCSEL is about 1000, indicating a good interfacial layer quality of the structure. The laser emits emission wavelength at 412 nm with a linewidth of 0.26 nm. The measurement results, including the linewidth reduction, degree of polarization of 79.4%, and the divergent angle of 5° are obtained. The laser has a threshold pumping energy of 784 nJ at room temperature and the characteristic temperature of 130K. Hakki-Paoli method was applied to analyze the temperature dependent optical gain and linewidth enhancement factor of the VCSELs. Due to the multiple cavity modes in the structure, the optical gain can be obtained by measuring the photoluminescence spectra below the threshold condition. At 80 K, the optical gain of 2.2×10^{3} cm^{-1} was estimated at the threshold condition with a carrier density of 6.8×10^{19} cm^{-3} by pulse laser. Under the different temperature, it is found that the gain increases more rapidly as a function of the injected carrier density at lower temperature. The α-factor at 80 K was estimated as 0.6 and increased to as high as 4.3 at 300K. The characterization of temperature dependent gain and α-factor provides further understanding in operation of the GaN-based VCSEL. Micro-PL intensity mapping indicated that the nonuniform PL emission intensity across the VCSEL aperture. The gain values of the highest PL intensity are larger than the ones of lower PL intensity. We obtained the sharp slope of gain spectrum from 400 nm to 420 nm while the slope of the gain spectrum ranging from 420 nm to 445 nm is smooth.

5.1.2 Cavity polariton dispersion in multimode GaN microcavity

The frequency spacing between adjacent PL peaks decreases by almost a factor of five from 470 nm to 370 nm. We use the material index dispersion and polariton dispersion to fit the experimental data, it shows that the latter fitting curve is much better than the former one. It is shown a very strong polariton dispersion in a multimode GaN surface emitting microcavity at room temperarure. There are multiple photon modes simultaneously in interaction with exciton. The dispersion in PL peaks can be described very well by the lower branch cavity polariton dispersion equation. The fitting gives an exciton-photon interaction constant is 290meV.

5.2 Future works

The DBR reflectivity has a roll off from 90% reflectivity at 383 nm to the first reflectivity minimum at 368 nm, as shown in Figure 4.3. The 4 μm bulk GaN layer has a PL peak at 365 nm with a linewidth of 7 nm. The Lorentzian roll off of GaN PL spectrum still has 7% of its peak value at 380 nm. The roll off of DBR reflectivity and that of the Lorentzian tail of GaN PL spectrum are in opposite directions but still have a overlap between 370 nm and 380 nm. Normally, this is not an optimized cavity reflectivity condition for investigating exciton-photon interaction. Therefore, we will fabricate the DBR with stop band center tuned to 370 nm and hope to measure the dispersion of upper and lower polariton branches.